The Design and Analysis of Bluff Body Dynamic Distortion Generators

Emily Padula

Thesis submitted to the Faculty of the

Virginia Polytechnic Institute and State University

in partial fulfillment of the requirements for the degree of

Master of Science

in

Mechanical Engineering

Alexandrina Untaroiu, Chair

K. Todd Lowe

Joseph Meadows

David Gonzales

May 12, 2025

Blacksburg, Virginia

Keywords: vortex shedding, dynamic distortion, StreamVane, bluff body, BeVERLI Hill

The Design and Analysis of Bluff Body Dynamic Distortion Generators

Emily Padula

(ABSTRACT)

With the increased use of serpentine diffusers in aircraft comes an increase in secondary flows and large pressure gradients which decrease engine efficiency. Therefore, in order to assess new engine technology, a way to generate these unsteady flows in ground test facilities needs to be developed. StreamVanes and ScreenVanes were developed at Virginia Tech as a way to generate real-world swirl and pressure distortion profiles for engine testing. However, they are only capable of generating steady distortion patterns, which limits the scope of inlet flow patterns that can be produced to evaluate various real-world scenarios. Therefore, this research study proposes the next generation of StreamVanes which are capable of generating dynamic distortion patterns in order to test the latest advances in aircraft engines.

Serpentine diffusers create unsteady flow in the form of counter-rotating vortices at the top dead center of the inlet. The frequencies associated with these dynamic distortion features that cause the most harm to the system are typically lower, on the scale of around one engine order. Knowing that, the goal of this research was to design a passive method to replicate this type of real-world flow based on existing literature on unsteady distortion and profile generation with StreamVanes. After extensive literature search, bluff bodies were identified as well-known geometries that create unsteady flow features, namely in the form of periodic, paired vortex shedding. Cylindrical bluff bodies create vortex streets that shed at a known frequency determined by their Strouhal number. BeVERLI Hill is a geometry that has been extensively studied by Virginia Tech due to its unique, asymmetric vortex

shedding that alternates chaotically off the back of the hill. Both of these types of bluff bodies were integrated with a base twin-swirl StreamVane design and were predicted to cause unsteadiness similar to the vortex pairs found in serpentine inlets. The designs underwent both computational tests and experimental tests in order to determine how they interact with the steady StreamVane flow pattern, how they scale with sizing and Mach number, and the frequency content of the unsteady flow features.

RANS/URANS CFD, flow visualization, and hot film anemometry were used to test the Dynamic StreamVane designs and gave results that provided a proof-of concept for this type of passive, unsteady distortion generator. From these results, it was found that the vortices were shed similarly to how they would if the bluff bodies were on their own, but as they continued downstream, they were carried in the direction of the flow from the twin swirl StreamVane and dissipated in their intensity past a diameter or two downstream. Additionally, there was evidence of the frequencies scaling with Mach number and bluff body size that aligned with expected relationships. Contrary to predictions, the frequency content did not indicate strong peaks at any particular frequencies. However, the majority of the energy was focused in the low frequency range, as desired. Further and more extensive testing of the designs is needed to fully understand how they can be used to generate specific dynamic distortion profiles at a given AIP, but this research provides a solid baseline from which to further develop the Dynamic StreamVane technology.

The Design and Analysis of Bluff Body Dynamic Distortion Generators

Emily Padula

(GENERAL AUDIENCE ABSTRACT)

With the increased use of curved air intakes in aircraft, known as serpentine diffusers, also comes the increase in non-uniform, time-varying air flow which decreases engine efficiency. Therefore, a way to generate these unsteady flows in ground test facilities needs to be developed in order to assess new engine technology. StreamVanes and ScreenVanes were developed at Virginia Tech as a way to generate specific flow distortion patterns. However, they are only capable to creating steady, not time-varying flow, which limits the scope of inlet flow patterns that can be produced for testing. Therefore, the next generation of StreamVanes is proposed that are capable of generating dynamic distortion patterns in order to test the latest advances in aircraft engines.

Serpentine diffusers create unsteady flow in the form of counter-rotating vortices at the top dead center of the inlet. The goal of this research was to design a simple method to replicate this type of real-world flow based on what is already known about unsteady flow and distortion profile generation with StreamVanes. After extensive literature search, bluff bodies were identified as well-known geometries that create unsteady flow features, namely in the form of periodic vortex shedding. Cylindrical bluff bodies create vortices that shed at a known frequency determined by their sizing and the speed of the flow. BeVERLI Hill is a geometry that has been extensively studied by Virginia Tech due to its unique, asymmetric vortex shedding that alternates chaotically off the back of the hill. Both of these types of bluff bodies were integrated with a steady StreamVane design and were predicted to cause

unsteadiness similar to the vortex pairs found in serpentine inlets. The designs underwent both computational tests and experimental tests in order to determine how they interact with the steady StreamVane flow pattern, how they scale with sizing and flow speed, and what frequencies the unsteady flow features exhibit.

Computational fluid dynamics and experimental flow visualization were used to test the Dynamic StreamVane designs and gave results that provided a proof-of concept for this type of passive, unsteady distortion generator. From these results, it was found that the vortices were shed similarly to how they would if the bluff bodies were on their own, but they were carried in the direction of the flow from the steady StreamVane and dissipated as they continued downstream. There was no evidence of any particular frequencies in the experimental tests, but the majority of the energy was in the low frequency range and the frequencies seemed to scale with the bluff body sizing and inlet velocity. Further and more extensive testing of the designs is needed to fully understand how they can be used to generate specific dynamic distortion profiles at a given location, but this research provides a solid baseline from which to further develop the Dynamic StreamVane technology.

Acknowledgments

First of all, I would like to thank my advisor, Dr. Alexandrina Untaroiu, for taking me on as a graduate student and introducing me to the the StreamVane group. Her guidance and support throughout the last two years have been a great asset to my journey through graduate school. I would also especially like to thank Dr. Todd Lowe for his support and expertise throughout the entirety of this project. He has been an invaluable resource for every step of the research process. I also cannot thank the rest of the StreamVane group enough, including Dr. Joe Gonzales, Will Eagan, Marcel Paris-Agafonov, and Grayson Groten, for their contributions to this project. They went above and beyond supporting this project, even if it meant coming into the lab with me well before sunrise.

I would also like to thank the Air Force Research Lab for sponsoring this project and providing the funding that allowed me to pursue this master's degree. Chase Nessler in particular was a great asset to the research, leading weekly meetings and providing guidance throughout the duration of the project. Additionally, I would like to thank Stephen Guillot and Cole Hefner at Techsburg, Inc. for collaborating with me on much of this project. It was a great experience to work along side them and develop this new StreamVane technology together.

Finally, I would like to thank my family and friends for getting me through a very tough two years. I would not have been able to continue through this work without their support and happy distractions. Thank you for everything!

Contents

List of Figures ix

List of Tables xiv

1 Introduction 1

2 Review of Literature 4

2.1 StreamVane Development 4

2.2 Cylindrical Bluff Bodies 6

2.3 BeVERLI Hill 9

3 Test Article Designs 14

4 Methodology 21

4.1 Computational Fluid Dynamics (CFD) 21

4.1.1 The RANS Equations 21

4.1.2 Computational Mesh 24

4.2 Experimental Testing 29

4.2.1 Flow Vizualization 30

4.2.2 Hot Film Anemometry 34

5 Results **37**

5.1 CFD Results 38

5.1.1 Steady CFD 38

5.1.2 Transient CFD 49

5.2 Experimental Results 54

5.2.1 Flow Visualization 54

5.2.2 Hot Film Anemometry 60

6 Conclusions **64**

6.1 Discussion of Results 64

6.2 Future Work 68

Bibliography **70**

List of Figures

1.1 Contour plots of the mean and RMS total pressure of a serpentine inlet run at Mach 0.691. Units are in psi. Figure reproduced from [2]. 2

1.2 Power spectral density function of the total pressure measurements in the vortex region of Figure 1.1. Figure reproduced from [21]. 2

2.1 Examples of StreamVanes based on HWB and bulk swirl inlet profiles 5

2.2 Regimes of fluid flow across smooth circular cylinders. Figure reproduced from [3]. 7

2.3 Karman-type verses Arch-type vortices. Figure reproduced from [20]. 8

2.4 Diagram of BeVERLI Hill. Figure reproduced from [5]. 10

2.5 Oil flow visualization of flow over the BeVERLI Hill in the 0 degree orientation. Figure reproduced from [5]. 11

2.6 Fluctuating pressure signals on the leeward side of the BeVERLI Hill. Figures reproduced from [18]. 13

3.1 (a) Streamlines and Tangential Flow Angle contour of a twin swirl distortion profile. Figure reproduced from [16]. (b) The twin swirl StreamVane design used as a base for the dynamic StreamVane designs. 15

3.2 Final test article geometries. 19

3.3 The additional StreamVane designs used for CFD. 20

4.1 Diagram of Mesh 2 from Table 4.1, which shows the mesh used for each CFD simulation. 27

4.2 y^+ values across the full StreamVane and bluff body. 28

4.3 The High-Speed Wind Tunnel (HSWT) at Virginia Tech. 30

4.4 Example of a 3D printed test article (the large BeVERLI Hill design). 31

4.5 Close up rendering of the test section for the flow visualization experiment . 32

4.6 Image of the test section for the flow visualization experiment 32

4.7 Close up rendering of the test section for the hot wire anemometry experiment. 35

4.8 Image of the test section for the hot wire anemometry experiment. Note that the section of the wind tunnel that is absent in this image was filled with 6"-diameter 3D printed spacers. They were removed for this photo to provide an easy visual of how the test article sits inside the test section. 36

4.9 TSI 1210-20 hot film sensor used for wind tunnel testing. [25] 36

5.1 (a) total pressure, (b) streamwise velocity, and (c) streamwise vorticity contours of the large square prism design at 1 inch downstream from the trailing edge of the StreamVane. The large square prism is located at the bottom dead center of the figures. 39

5.2 (a) total pressure, (b) streamwise velocity, and (c) streamwise vorticity contours of the small square prism design at 1 inch downstream from the trailing edge of the StreamVane. The small square prism is located at the bottom dead center of the figures. 39

5.3 (a) total pressure, (b) streamwise velocity, and (c) streamwise vorticity contours of the large square prism design at 6 inches (1 diameter) downstream from the trailing edge of the StreamVane. The large square prism is located at the bottom dead center of the figures. 40

5.4 Total pressure loss coefficient of the large square prism geometry at 1 diameter downstream. 41

5.5 Contours of the large square prism located at the top dead center of the StreamVane. (a), (b), and (c) are located 1 inch downstream from the trailing edge of the StreamVane. (d), (e), and (f) located 6 inches (1 diameter) downstream from the trailing edge of the StreamVane. 42

5.6 Contours of the BeVERLI Hill located at the top and bottom dead center of the StreamVane. (a), (b), and (c) are located 1 inch downstream from the trailing edge of the StreamVane. (d), (e), and (f) located 6 inches (1 diameter) downstream from the trailing edge of the StreamVane. 44

5.7 Contours across the surface of the BeVERLI Hill located at the bottom dead center of the StreamVane. (d) from [5] serves as a comparison to (c) 45

5.8 (a) streamwise vorticity and (b) skin friction coefficient contours from the top down view of the computational domain of the large BeVERLI Hill design. . 46

5.9 (a) streamwise vorticity and (b) skin friction coefficient contours from the bottom up view of the computational domain of the large BeVERLI Hill design. 47

5.10 Total pressure loss coefficient of the BeVERLI Hill geometry at 1 diameter downstream. 47

5.11 (a) streamwise vorticity and (b) skin friction coefficient contours from the top down view of the computational domain of the large square prism design. . . 48

5.12 A time series of velocity contours of the large square prism design at 0.5in above the base of the shroud. These are oriented so the inlet is at the top and outlet is at the bottom. 49

5.13 A time series of velocity contours of the large square prism design at the cross section 1 diameter downstream. 50

5.14 Velocity vs time in the vortex shedding region of the large square prism geometry. 50

5.15 A time series of velocity contours of the small square prism design at 0.5in above the base of the shroud. These are oriented so the inlet is at the top and outlet is at the bottom. 51

5.16 Velocity vs time in the vortex shedding region of the small square prism geometry. 52

5.17 A time series of velocity contours of the BeVERLI Hill design at 0.5in above the base of the shroud. These are oriented so the inlet is at the top and outlet is at the bottom. 53

5.18 Velocity vs time in the vortex shedding region of the BeVERLI Hill geometry. 54

5.19 Variance contours of two separate runs at Mach 0.45 with the large square prism bluff body. Each is mean-subtracted and first mode-subtracted. 56

5.20 Variance contours of a run at Mach 0.45 with the small square prism bluff body. It is mean-subtracted and first mode-subtracted. 56

5.21 Snapshots from a run at Mach 0.45 with the large square prism bluff body. These are sequential frames showing the bottom vortex moving outward along the wall away from the bluff body over time. 57

5.22 The power spectral density of a large square prism run at Mach 0.45 in the region of the bottom shedding vortex. 58

5.23 The power spectral density of a large square prism run at Mach 0.45 in the region of the top shedding vortex. 59

5.24 The power spectral density of a small square prism run at Mach 0.45 in the region of the top shedding vortex. 59

5.25 The sampling locations centered around the BeVERLI hill, 20 degrees to the left and 10 degrees to the right, and their Mean Velocity and U'/U_∞ values at Mach 0.45. 60

5.26 PSD of a low variance region verses a high variance region. 61

5.27 The sampling locations centered around the BeVERLI hill, 10 degrees to the left and 10 degrees to the right, and their Mean Velocity and U/U_∞ values at Mach 0.35. 62

5.28 PSD of a low variance region verses a high variance region in the Mach 0.35 case. 63

List of Tables

3.1 This table displays the sizing parameters for each test article. The width is displayed as a fraction of the 6" duct diameter. The frequency of vortex shedding is displayed as a fraction of engine order. Note that due to the chaotic nature of BeVERLI Hill, the average frequency values carry no real significance. 16

4.1 The sizing parameters associated with each grid level. 25

4.2 The results from the grid convergence study, looking at the integral values of the mass flow rate, turbulent kinetic energy, and turbulent viscosity at 1 diameter downstream of the trailing edge of the StreamVane. 26

List of Abbreviations

λ	thermal conductivity
μ	dynamic viscosity
ω	turbulence specific dissipation rate
ω_z	streamwise vorticity
ρ	density
τ	stress tensor
AIP	Aerodynamic Interface Plane
APPL	Advanced Propulsion and Power Laboratory
CFD	Computational Fluid Dynamics
DNS	Direct Numerical Simulation
e	internal energy
E_t	total energy
f	frequency
FVM	Finite Volume Method
h	specific enthalpy
H_t	enthalpy

HWB Hybrid Wing Body

HWST High Speed Wind Tunnel

k turbulent kinetic energy

L characteristic length

LDV Laser Doppler Velocimetry

LES Large Eddy Simulation

OFI Oil Film Interfereomtry

p pressure

p_t total pressure

PIV Particle Image Velocimetry

PSD Power Spectral Density

q heat flux vector

R specific gas constant

RANS Reynolds Averaged Navier Stokes

Re Reynolds Number

RMSE Root Mean Squared Error

SLA Stereolithography

SPOD Spectral Proper Orthogonal Decomposition

St Strouhal number

T temperature

t time

U_∞ freestream velocity

URANS Unsteady Reynolds Averaged Navier-Stokes

w streamwise velocity

Chapter 1

Introduction

The current uses of StreamVane and ScreenVane technology have proven to be effective in generating steady swirl and pressure distortion patterns at a defined Aerodynamic Interface Plane (AIP). They have been used to test engine fans and compressors against real-world, nonuniform flow regimes that often cause stress to turbomachinery [14]. Instead of producing generic swirl and pressure profiles like other flow control devices, StreamVane technology is able to take a complex profile and design a vane pack that will reproduce that specific profile for ground testing. This means turbomachinery is able to be tested under real-world flight conditions simply by installing a passive flow control device upstream of the engine.

While StreamVanes continue to be a great asset to the aerospace community, recent innovations in the aerospace industry have created a need for a new generation of distortion generators that produce dynamic distortion patterns. There has been increased manufacturing of jet engines that utilize S-duct diffusers to improve aerodynamic efficiency [17]. This new generation of aircraft focuses on creating higher thrust to weight ratios, which requires shorter airframes with compact S-ducts known as serpentine diffusers. The complex curvature of the serpentine diffuser creates large, fluctuating pressure gradients which generate secondary flows in the form of counter-rotating vortices, as can be seen in the top dead center of Figure 1.1 [2]. When taking the power spectral density of the vortex region (Figure 1.2), the peak energy occurs at frequencies around 300Hz, which corresponds to an engine order of about 1 for this setup, where engine order refers to the number of fluctuations per

revolution of the engine fan [21]. This unsteady behavior decreases engine efficiency and reduces compressor stability [17]. Therefore, there is a need to test engines, fans, and compressors against these unsteady flow patterns. The development of Dynamic StreamVanes has become the clear next step in advancing StreamVane technology in order to understand and improve the latest aircraft advancements.

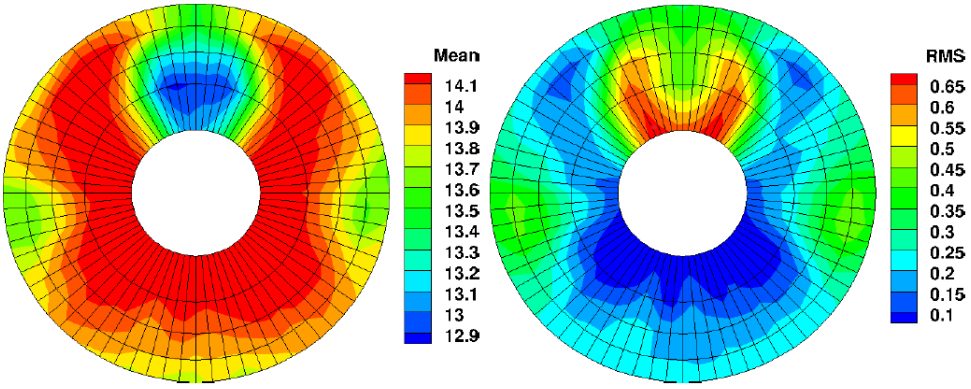

Figure 1.1: Contour plots of the mean and RMS total pressure of a serpentine inlet run at Mach 0.691. Units are in psi. Figure reproduced from [2].

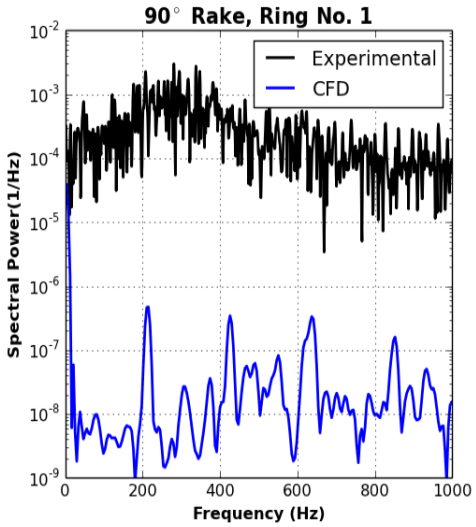

Figure 1.2: Power spectral density function of the total pressure measurements in the vortex region of Figure 1.1. Figure reproduced from [21].

One benefit of current, steady StreamVanes is they are a completely passive technology.

They can be easily placed in any wind tunnel at an engine test facility and generate a defined distortion profile at the AIP. Other versions of inlet distortion generators often use active approaches, such as airjets [15]. However, they are much more difficult to implement in a wide range of test facilities. Therefore, the present work focuses on designing Dynamic StreamVanes that generate unsteadiness using passive means. After extensive literature search, the use of bluff bodies to introduce dynamics into the system gained the greatest traction and is what is explored in this current study.

The overarching goal of this research is to design and test prototypes for a Dynamic StreamVane that utilizes the known flow dynamics of bluff bodies to generate unsteady distortion patterns that correspond to real-world engine applications. This will provide a proof of concept for the use of passive distortion generators to produce unsteadiness in a desired location and at desired frequencies, while integrating them into a given mean flow pattern. The effectiveness of the Dynamic StreamVane designs is determined by analyzing the energy and frequency content of the bluff-body distortion, determining the scalability of the unsteadiness with Mach number and bluff body size, and understanding how the dynamic flow patterns integrate with the mean flow pattern from a StreamVane. Evaluating each of these objectives will provide a strong foundation for future development of Dynamic StreamVane technology, with the ultimate goal of being able to produce a given profile at a specified AIP that contains unsteadiness with a defined frequency, pattern, and location.

Chapter 2

Review of Literature

2.1 StreamVane Development

StreamVanes were developed by a team at Virginia Tech to fulfill a need for a new technique that generates swirl distortion for the testing of jet engines [14] [13] [8]. Inlet flow distortion has been a continuing problem for the performance of turbofan engines. When the flow is distorted, fan and compressor blades pass through regions of flow that they were not originally designed for. These nonuniform regions of flow can cause vibrations and increased stress on the turbomachinery, decreasing the blade performance, and lowering the engine surge margin and efficiency [14]. Therefore, there is a need to generate these distortion patterns in wind tunnels and engine test cells in order to create engines that are tolerant to different levels of swirl distortion. Previous methods were only able to generate generic swirl patterns, rather than reproduce distortion profiles from particular flight scenarios. However, with the development of the StreamVane Design Method, we are able to design a passive flow control device that can produce any given swirl pattern.

The StreamVane Design Method takes a desired swirl profile and generates a vane pack where NACA 63-006 profile turning vanes are strategically placed perpendicular to the flow. They are then structurally secured with support vanes and attached to a shroud in 3D CAD software. The designs are additively manufactured, which allows for more precision, short manufacturing time, and the ability to manufacture more complex designs. Since the desired

swirl profile is needed on a plane downstream of the StreamVane (at the AIP), the low-fidelity model, StreamFlow, was developed to predict how flow propagates downstream. In practice, the StreamFlow model can place the desired profile at the "outlet" and calculate how flow evolves upstream to the plane at the trailing edge of the StreamVane and design a vane pack based on that upstream profile [23]. Therefore, the distortion generated by the StreamVane creates the desired profile at the AIP, rather than at the trailing edge of the vanes.

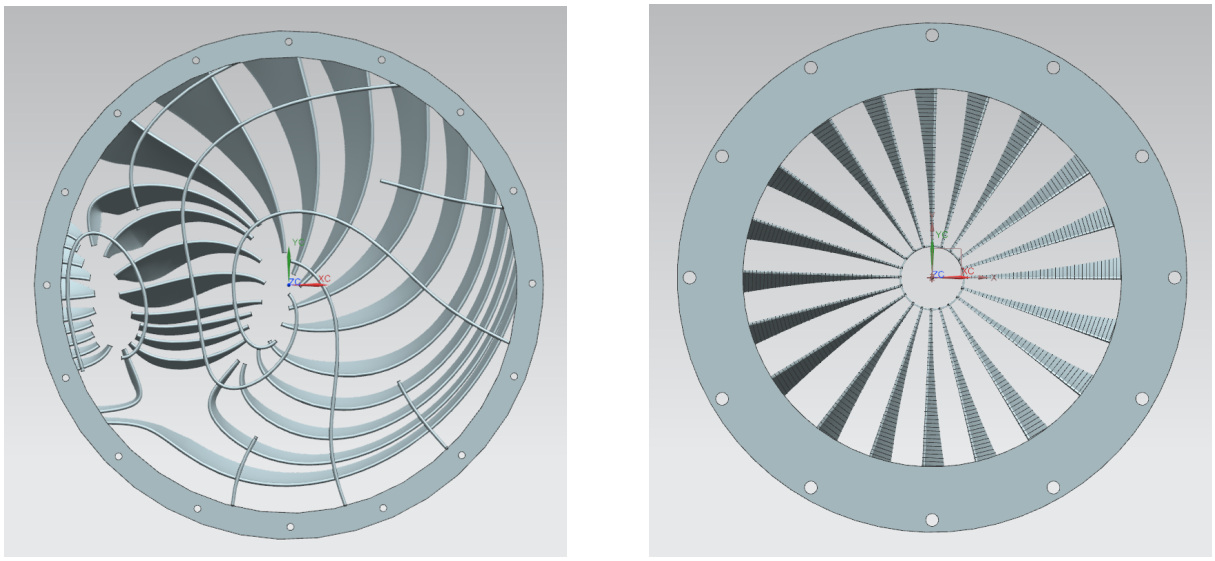

(a) HWB (b) Bulk Swirl

Figure 2.1: Examples of StreamVanes based on HWB and bulk swirl inlet profiles

The StreamVane designer has been computationally and experimentally verified for a variety of different applications. In an initial investigation of the StreamVane Design Method by Hoopes, a 5-hole probe was used to measure the swirl angle profile of various StreamVane designs and compare it the goal profile to determine the accuracy of the distortion generator [14]. Bulk swirl, twin swirl, serpentine inlet, and HWB inlet profiles were all designed and tested. The difference between the experimental profile and the goal profile was measured using the RMSE value of the swirl angle. Each design had RMSE values below 7 degrees, and the simpler bulk and twin swirl patterns were even within the range of the experimental

uncertainty of the 5-hole probe [14]. This indicates that the StreamVane distortion generator is sufficiently accurate in generating a desired swirl profile at a given AIP. StreamVanes have also been tested to verify their structural integrity and flutter conditions. Researchers looked at parameters such as Reynold's number, vane turning angle, and vane trailing edge thickness and tested how each impacts the structural stability of the StreamVane [11]. Both a hybrid RANS and LES approach and time-resolved particle image velocimetry (PIV) measurements were compared and evaluated to determine whether there is risk of structural failure [12]. It was found that the vortex shedding modes from the trailing edge of the vanes contained frequencies much higher than the dominant structural modes, so vortex induced vibrations are unlikely to occur [10]. Since StreamVanes have passed assessments for both accuracy and structural integrity, they have proven their worth in generating steady distortion patterns. The next iteration of StreamVanes will need to take what is known of the steady StreamVane design and use it to expand into dynamic distortion generation.

2.2 Cylindrical Bluff Bodies

Flow around bluff bodies has been studied for a long time due to its prevalence in everyday life and its challenging vortex shedding dynamics. The dynamics of the flow behind a bluff body greatly depends on the Reynolds number of the flow. The various flow regimes are depicted by Dalton in Figure 2.2 with the general Reynolds number ranges where each occur [3]. At very low Re, the flow remains unseparated, but as the Re increases, a separation region forms behind the cylinder and steady, symmetric vortices form. As the Re increases even higher, the recirculation region behind the bluff body grows, and the Re eventually reaches a critical value where the vortices become unstable. This produces periodic oscillation in the form of a vortex street, where the vortices shed alternately in an anti-symmetric wake

pattern known as a Karman vortex street [24]. The vortices form because of an adverse pressure gradient that is produced at the base of the body. The boundary layer is forced to separate and produce vortices that stretch around the body in a horseshoe shape and are then carried continuously downstream in pairs [20].

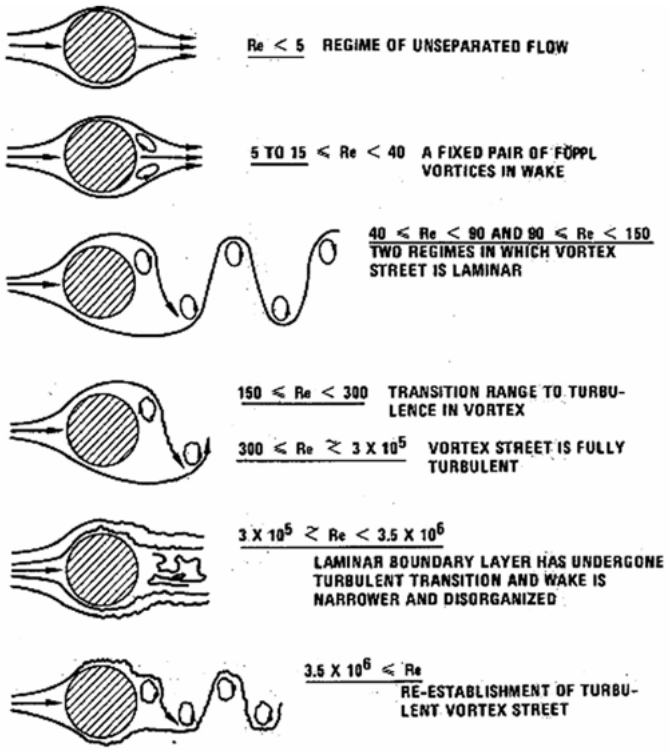

Figure 2.2: Regimes of fluid flow across smooth circular cylinders. Figure reproduced from [3].

The current study is focused on the high Re ranges where turbulent vortex streets are formed. As mentioned, these often take the form of a Karman vortex street. However, it has been found that for certain aspect ratios, cylinders can also produce arch-type vortices. Karman vortices shed alternately downstream, while arch-type vortices shed in parallel, as shown in Figure 2.3 [20]. For circular cylinders, this transition from Karman to arch-type vortex streets occurs below an aspect ratio of $h/d = 2.5$, where h is the height and d is the diameter. For square prisms, it occurs below $h/w = 2.0$, where w is the width of the square [20]. This

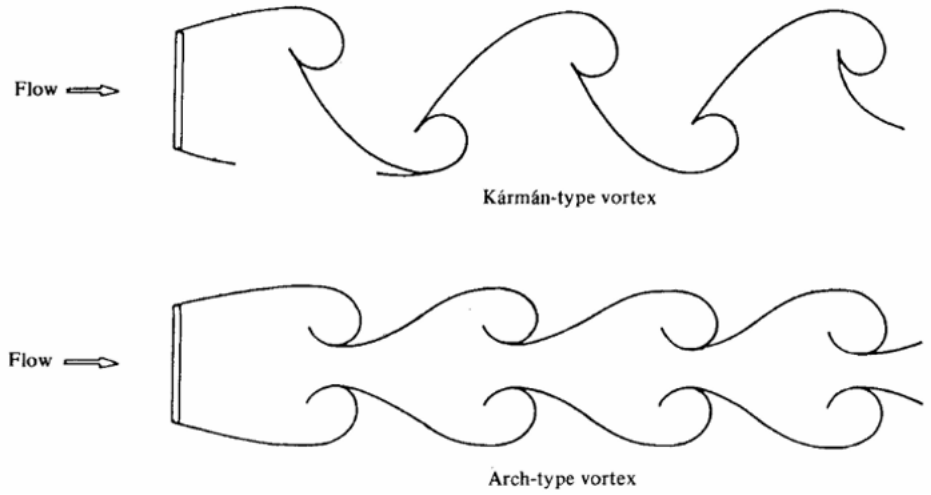

Figure 2.3: Karman-type verses Arch-type vortices. Figure reproduced from [20].

likely occurs because when the aspect ratio is larger (the height is large compared to the width), the flow separating from the sides is stronger than the flow separating from the top, so the wake is mostly controlled by the sides and Karman type vortices occur. When the width is increased, the flow separating from the top joins the flow from the sides and forms arch-type vortices [20]. When the aspect ratio reaches 1.5 for circular cylinders and 1.0 for square prisms, no prominent frequencies are detectable anymore. The frequencies at which the vortices shed is dictated by the Strouhal number, $St = \frac{fL}{U_\infty}$, where f is the shedding frequency, L is the characteristic length scale, and U_∞ is the freestream velocity. Many experiments and computational simulations have been conducted to determine the Strouhal number at various Re and bluff body shapes. Most sources have concluded that in the Reynolds number regime on the order of 1×10^5, the Strouhal number plateaus at about 0.2 for circular cylinders and about 0.12 for square cylinders [22]. With these relationships in mind, the sizing of the bluff bodies used in the Dynamic StreamVane designs were decided in order to produce each type of vortex shedding at the desired frequency range of about 1 engine order. The specifics of these sizing decisions will be further discussed in Section 3.

2.3 BeVERLI Hill

The BeVERLI Hill (Benchmark Validation Experiments for RANS and LES Investigations) geometry was created as part of a collaborative effort between Virginia Tech, NASA, and a few other organizations and academic institutions to establish a benchmark validation set for CFD solvers [5]. Both experimental and computational research has been conducted across a range of facilities to provide a complete validation test case in order to further understand the simulation capabilities and underlying physics for problems involving 3D non-equilibrium turbulent boundary layers [18]. Flow separation is well known to be a weak point in RANS linear eddy-viscosity models, so it is important to establish a complete validation set in order to understand the complete capabilities of RANS and LES solvers [4] [9]. The BeVERLI Hill geometry was selected because of its ability to generate a complex flow field with pressure gradients, curvature effects, boundary layer separation, and large-scale unsteadiness, while still having a relatively simple numerical and experimental setup [6] [9] [18]. CFD and wind tunnel tests were conducted at low Mach numbers and a range of high Reynolds numbers across multiple facilities to assess the sensitivity of the flow to manufacturing errors, inflow conditions, and grid nonuniformities [5] [6]. Experiments included measuring static pressure across the hill, Laser Doppler Velocimetry (LDV) to measure the turbulent boundary layer, PIV, and oil flow visualization to look at skin friction [6]. RANS simulations were performed using different grids, solvers, and turbulence models to study their effects on the numerical solution and how closely they match experimental results [4]. While this investigation is still ongoing, the flow features that result from the BeVERLI Hill exhibit valuable dynamics that could be harnessed in the context of Dynamic StreamVanes.

The BeVERLI Hill geometry is defined by a 5th degree polynomial centerline profile, where its first and second order derivatives are zero at the peak and base [5]. The two 5th degree polynomials cross at the top of the hill, creating a square, flat top and superelliptic corners at

the base. This forms a hill with two unique, symmetric orientations. The 0 degree orientation is defined when the 5th order polynomial profile faces the oncoming flow, while the 45 degree case is a 45 degree rotation from this, so the corner of the base faces the oncoming flow [18]. The 0 degree case has an aspect ratio of $w/h = 2.3$, while the 45 degree case has an aspect ratio of $w/h = 3.4$ [26]. A diagram of this geometry can be seen in Figure 2.4.

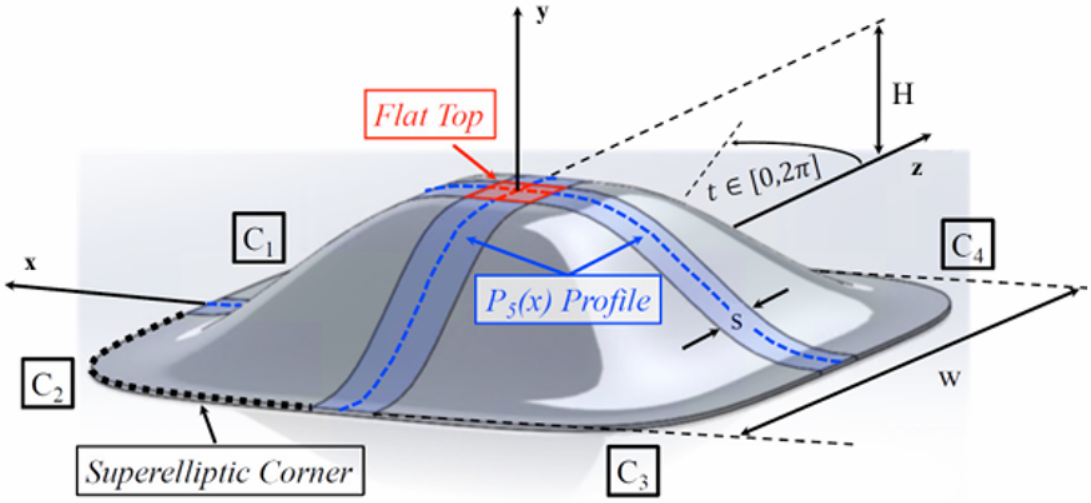

Figure 2.4: Diagram of BeVERLI Hill. Figure reproduced from [5].

Wind tunnel tests were run for Reynolds numbers between 250,000 and 650,000 for both 0 degree and 45 degree orientations and compared to RANS simulations with similar boundary conditions [5]. For each orientation, a stagnation point occurs at the front of the hill, and the flow experiences a large favorable pressure gradient, indicating a complex shear layer at the top of the hill [5]. A large separation bubble then appears in the large adverse pressure gradient region of the wake [5]. While both orientations are symmetric, the measurements showed that the resulting flow is actually asymmetric [5]. This is visible in the wake of the hill where two counter-rotating vortices are skewed asymmetrically to one side [5]. For the 0 degree case, this asymmetric wake is actually unstable and switches sides chaotically [6]. The instability is seen in the unsteady pressures along the radial $\pm 45°$lines of the hill that

are almost exactly out of phase, as is shown in Figure 2.6a [6] [7] [18]. This switching occurs on very long timescales (on the order of a few seconds), which is much longer than typical vortex shedding timescales [7] [18] [26]. This large timescale reflects how the phenomenon has very low probability and is highly sensitive to irregularities. It also does not have a distinct switching frequency. The timescales can be orders of magnitude above or below the average, which makes the mean value hold very little weight [18]. Despite the chaotic nature of the switching, the Strouhal number was confirmed to be about 0.003, using the width, the freestream velocity, and the approximate oscillation frequency [6].

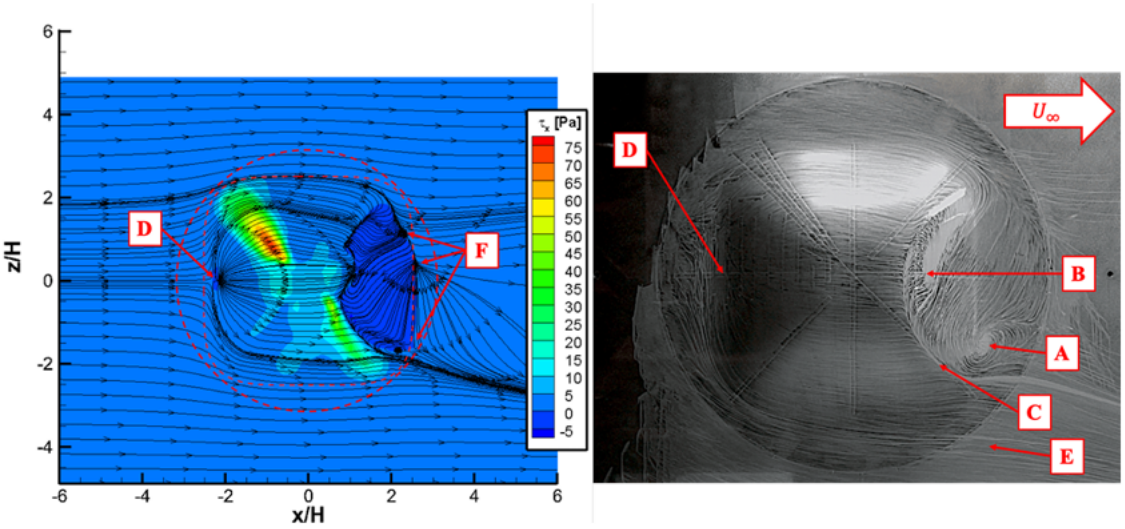

Figure 2.5: Oil flow visualization of flow over the BeVERLI Hill in the 0 degree orientation. Figure reproduced from [5].

The 45 degree orientation also exhibits asymmetric flow in its wake, especially as the Reynolds number increases, but there is no evidence of any bistability or chaotic switching [26] [6] [18] [9]. These asymmetries occurred across multiple facilities and were present in RANS simulations with perfectly symmetrical boundary conditions and meshes, indicating that this is likely not due to imperfections of the facilities or CFD grids as originally hypothesized [5]. The asymmetry appears to be an inherent characteristic of the flow, due

to the shear layer instabilities that arise from the interaction of the boundary layers over the top and sides and converging on the leeward side of the hill [9] [7].

Although both the 0 degree and 45 degree cases exhibit this surprising asymmetry resulting from their symmetric geometry, the 0 degree case is of largest importance to the present study because of its unsteady nature. This chaotic, unstable vortex switching is very different from that seen in standard bluff body vortex shedding described previously with cylinders [7]. The timescales of the unsteadiness is much longer than the typical sampling period of experiments or computations [26]. To replicate the real world dynamic distortion patterns found in modern serpentine inlets, the frequencies of unsteadiness that are of importance are low frequencies, on the order of 1 engine order, because those fluctuations cause the most instability in the turbomachinery. Therefore, the fact that the chaotic switching phenomenon of BeVERLI Hill occurs on such long timescales is of great interest.

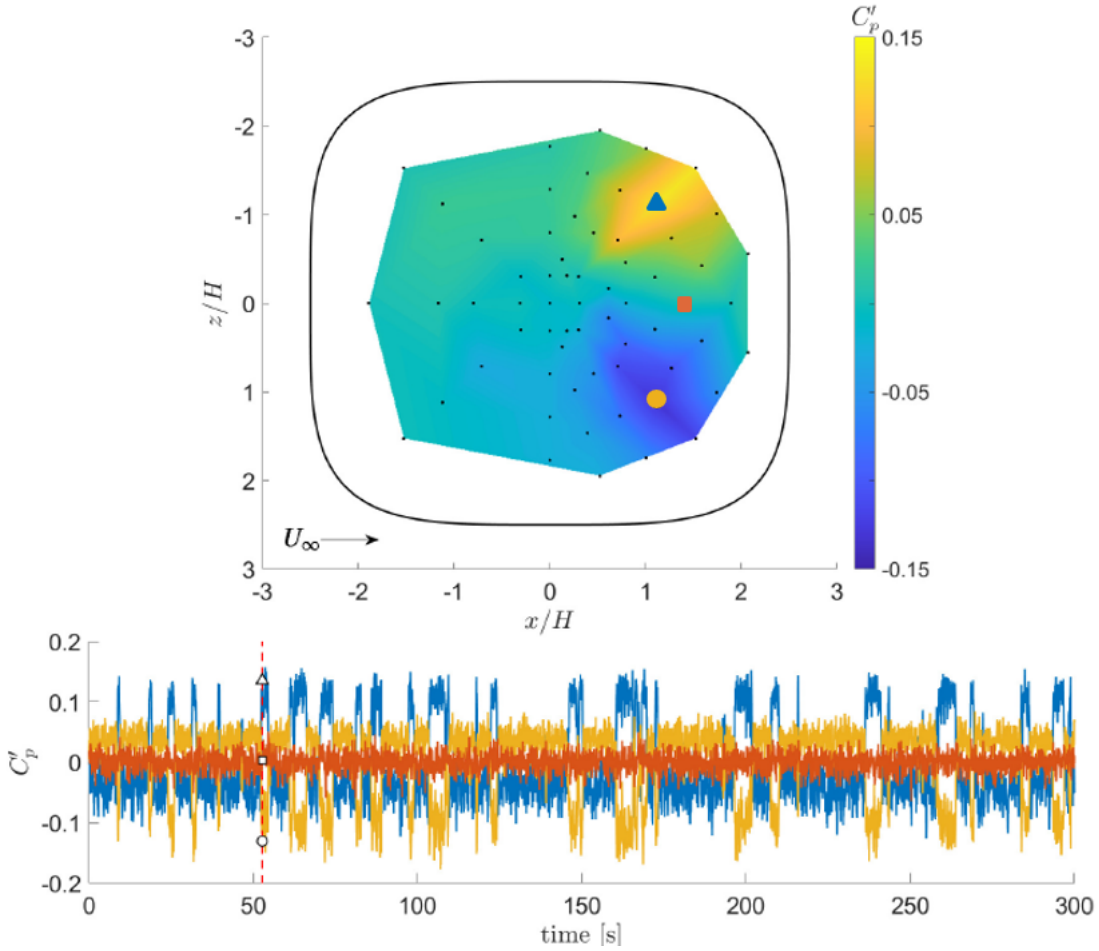

(a) Fluctuating pressure field at the back side of the 0 degree orientation hill, with Re = 250k. The signals of the three labeled ports are shown in the time trace below the figure.

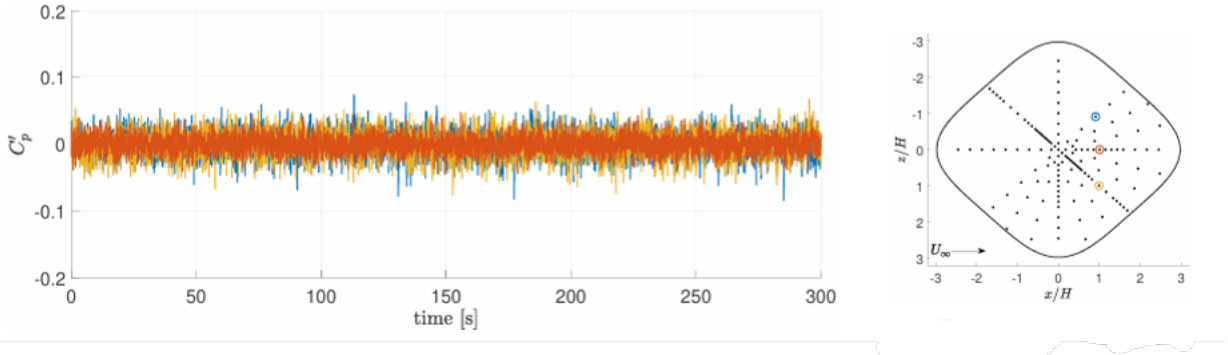

(b) The time trace of the fluctuating pressure signals from the three pressure taps on the 45 degree orientation BeVERLI Hill at Re = 250k.

Figure 2.6: Fluctuating pressure signals on the leeward side of the BeVERLI Hill. Figures reproduced from [18].

Chapter 3

Test Article Designs

One of the goals of this study is to determine how the dynamic flow features from the bluff bodies interact and evolve once integrated into an overall, steady StreamVane distortion pattern, so a simple base pattern was chosen to allow for easier analysis of this interaction. The counter-rotating twin swirl is a well-known distortion profile that also has great relevance to S-ducts and is depicted in Fig 3.1a. As previously mentioned, the inlet distortion pattern of serpentine diffusers consists of fluctuations at the AIP which were mainly attributed to the oscillation of twin vortices at the top dead center [2]. Copenhaver found that these fluctuations were largely broadband, but the largest power was associated with about 300Hz (as displayed previously in Figure 1.2). For the size of the duct used in the study, 17", this roughly corresponds to the rotational speed of the fan, or one engine order. Since this flow pattern has great significance to a relevant application, a twin swirl was established as a good baseline pattern. A twin swirl pattern is also very well-known and well-tested by the Virginia Tech team and the SteamVane Design Code, having been studied and verified at the very beginning stages of the design code [14]. Its simplicity will make it easier to detect how the distortion from the bluff bodies may be carried by the steady StreamVane pattern.

The square prism bluff bodies were sized to easily integrate with the base StreamVane design, while also producing a dominant shedding frequency corresponding to an engine order of 1 or 2. The reference used to establish the relevant frequencies that correspond to those engine orders was an engine fan rotating at about Mach 1. For a 6" fan rotating at Mach 1, an

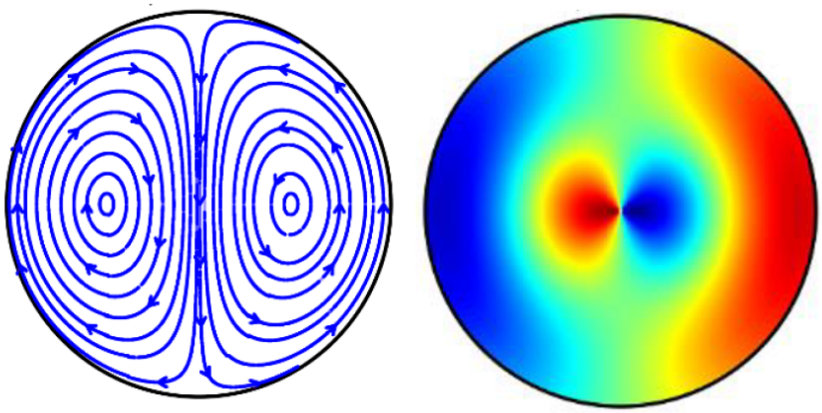

(a)

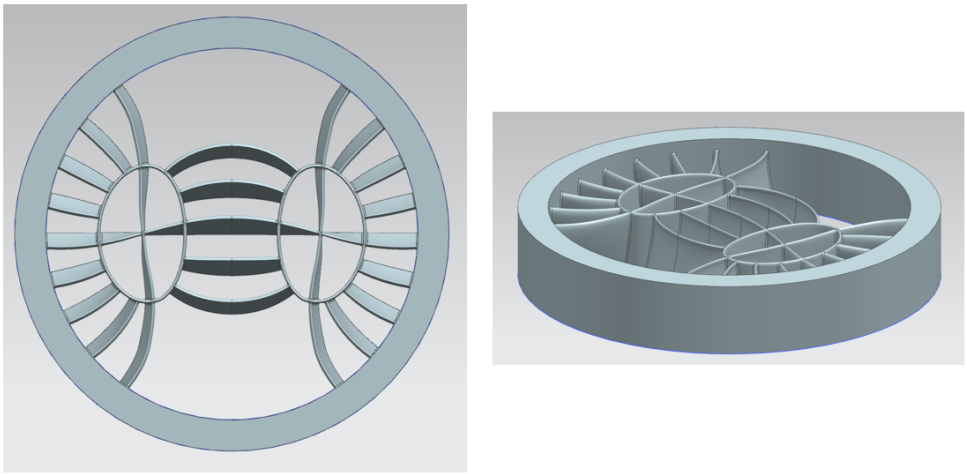

(b)

Figure 3.1: (a) Streamlines and Tangential Flow Angle contour of a twin swirl distortion profile. Figure reproduced from [16]. (b) The twin swirl StreamVane design used as a base for the dynamic StreamVane designs.

engine order of 1 is equivalent to approximately 700 Hz and an engine order of 2 is equivalent to about 1400 Hz. The Strouhal number of square prisms is estimated to be about St = 0.12 [22], and is used to calculate the characteristic length needed to attain the frequency of one engine order with the following equation,

$$St = \frac{fL}{U_\infty}, \qquad L = St\frac{U_\infty}{f} \tag{3.1}$$

where f is the vortex shedding frequency, L is the characteristic length (width of the prism), and U_∞ is the free-stream velocity. A Mach number of 0.4 was used for the free-stream velocity because it roughly aligns with the test conditions used for the wind tunnel tests and aligns with the Mach numbers that are relevant for real-world applications. These square prism widths are reflected in Table 3.1 as a fraction of the circumference of a 6" StreamVane.

Table 3.1: This table displays the sizing parameters for each test article. The width is displayed as a fraction of the 6" duct diameter. The frequency of vortex shedding is displayed as a fraction of engine order. Note that due to the chaotic nature of BeVERLI Hill, the average frequency values carry no real significance.

	Bluff Body	Width/Circumference	Frequency (per engine order)	Aspect Ratio	Blockage
a	Square Prism	0.048	0.95	1.25	3.6%
b	Square Prism	0.024	1.9	2.25	1.6%
c	BeVERLI Hill	0.053	0.0215	2.3	0.59%
d	BeVERLI Hill	0.127	0.009	2.3	2.4%

As mentioned in the literature review, the aspect ratio of the prisms dictates whether they produce Karman-type or arch-type vortices. Aspect ratios between 1 and 2 are predicted to produce arch-type vortices while aspect ratios above 2 are predicted to produce Karman-type vortices. Both vortex types produce interesting, paired vortices that could be of use when reproducing specific dynamic distortion patterns. Therefore, the aspect ratios displayed in Table 3.1 were chosen so both vortex types would be represented. The final designs of these two sizings integrated with the twin-swirl StreamVane is shown in Figure 3.2.

For the BeVERLI Hill StreamVane designs, there is not as clear of a relationship between the sizing and vortex shedding behavior as there is in the square prism cases. The dynamic switching that the 0 degree BeVERLI Hill exhibits is extremely chaotic, so the Strouhal number cannot be used as an exact predictor of its frequency. Instead, the Strouhal number

relationship merely gives an average switching frequency, when in reality, the timescales of the switching can be orders of magnitude above and below this value. Since the switching frequency is unpredictable, the sizing was mainly a compromise between making it small enough to integrate well with the StreamVane without causing too much blockage, while still being large enough to create an adequately sized wake that will be evident downstream. Additionally, the BeVERLI Hill on the vane was sized to exactly fit on the width of the center vane. The final widths as a fraction of the circumference, as well as the mean frequency as a fraction of engine order are recorded in Table 3.1.

Three out of the four chosen geometries have the bluff body attached to the wall of the shroud. This aligns with the location of the dynamic distortion that occurs in a serpentine duct, as shown in Figure 1.1, where the paired vortices occur near the wall at the top dead center. However, for the BeVERLI Hill, this poses a slight issue because, until this study, the BeVERLI Hill had only been assessed on a rectangular duct, so it would lie flush with the wall. For obvious reasons, its flat base cannot lie exactly flush with the curved wall of the shroud. Therefore, the decision was made to have the center of the base of the hill lie flush with the center of the inner wall of the StreamVane, so some of the geometry is cut off where the curvature of the wall intersects the hill. It is unclear how that may affect the dynamics of the separation region, but it is not predicted to cause too much of an issue since it is only a minor amount that gets cut off. The fourth and final design has the BeVERLI Hill attached to a center vane with a hill above and below the vane to add stability. This will allow the exploration of how vortices from the two hills interact with each other and with the twin-swirl pattern when placed at an alternate location. It is predicted that it may create more of a chaotic quad-swirl formation due to the two vortices formed by the top hill and the two vortices formed by the bottom. However, it is important to note that these BeVERLI hills are much smaller in scale than those previously tested by Virginia Tech, so

the vortices may not be as strong as the size decreases.

In addition to the four designs that were printed for experimental testing, two more designs were added for CFD testing. These were added as a means to understand how the location of the bluff body within the StreamVane effects the interaction of the vortices with the main, twin-swirl flow. The first additional design used the same large square prism but placed it at the opposite side of the StreamVane, as shown in Figure 3.3a. With this design, we will be able to compare how the positioning of the bluff body relative to the StreamVane flow changes the dynamic distortion pattern. Similarly, the second additional design added a BeVERLI Hill on the opposite side of the StreamVane, as shown in Figure 3.3b. This means one CFD run will be able to give insight into both bluff body positions, saving computational resources.

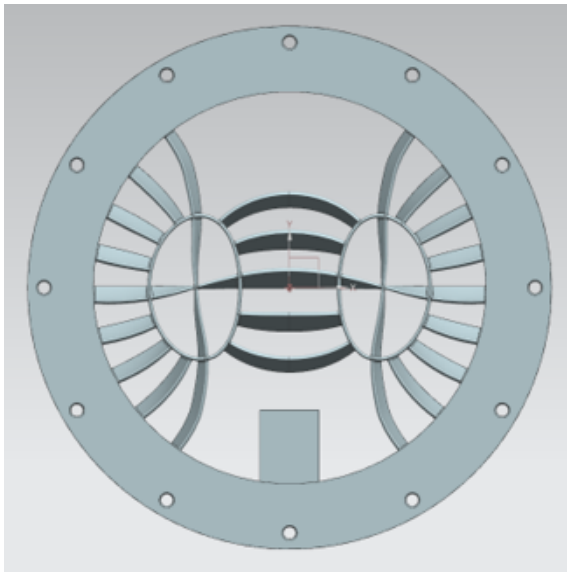

(a) Large Square Prism

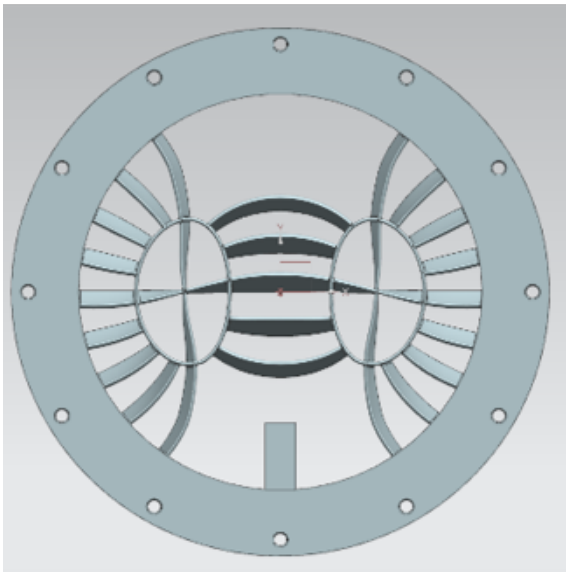

(b) Small Square Prism

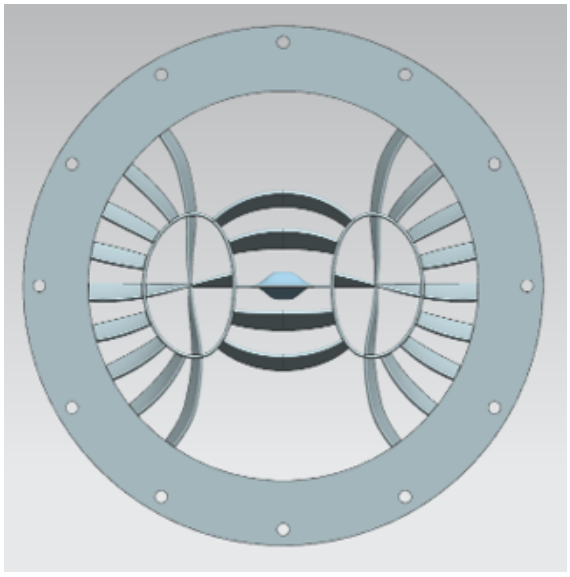

(c) BeVERLI on a vane

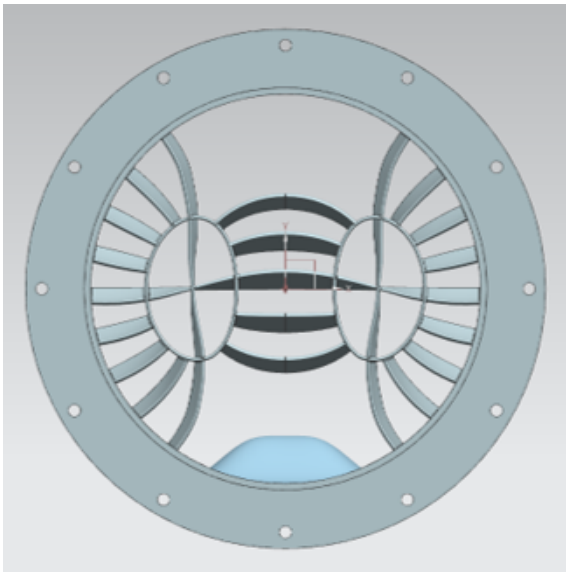

(d) Large BeVERLI

(e) Side view of (a), (b), and (c)

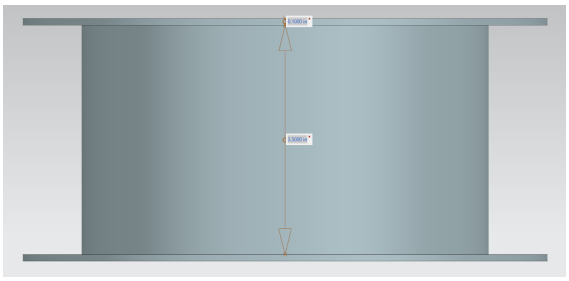

(f) Side view of (d)

Figure 3.2: Final test article geometries.

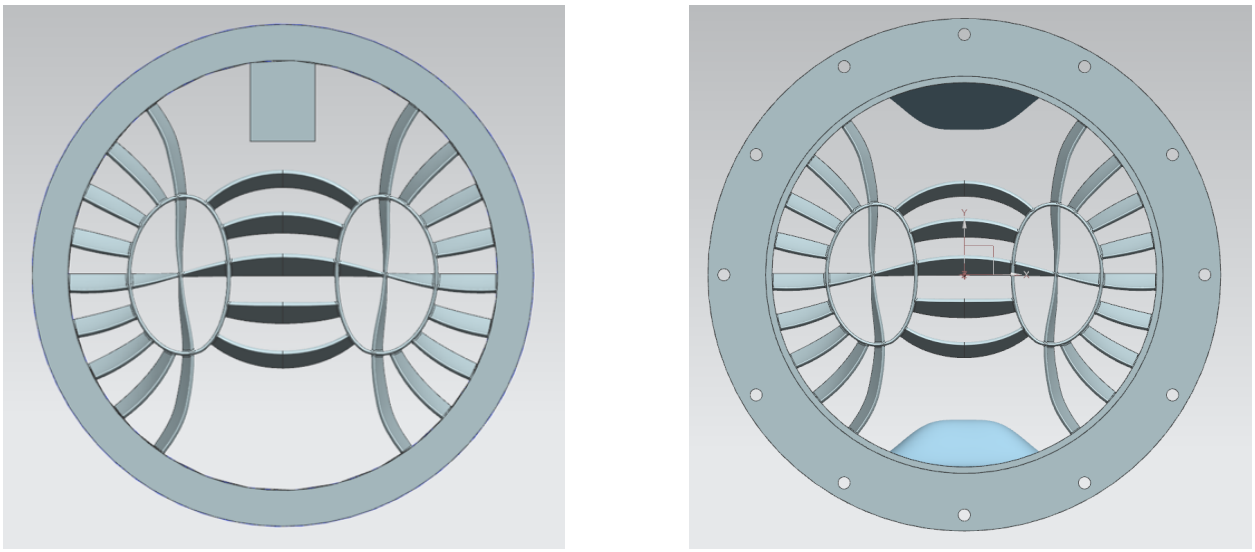

(a) Large Square Prism at the top.

(b) Double BeVERLI Hills

Figure 3.3: The additional StreamVane designs used for CFD.

Chapter 4

Methodology

4.1 Computational Fluid Dynamics (CFD)

4.1.1 The RANS Equations

The CFD simulations were conducted using ANSYS Fluent software, which utilizes the finite volume method (FVM) to solve the Reynolds Averaged Navier-Stokes (RANS) equations [1]. The RANS equations are commonly used to describe turbulent flows since they use Reynolds decomposition to separate the mean, time-averaged flow component from the fluctuating flow component. They are derived from the instantaneous compressible Navier-Stokes equations, detailed below in conservation form [1].

$$\frac{\partial \rho}{\partial t} + \frac{\partial}{\partial x_j}(\rho u_j) = 0 \tag{4.1}$$

$$\frac{\partial}{\partial t}(\rho u_i) + \frac{\partial}{\partial x_j}(\rho u_j u_i) = -\frac{\partial p}{\partial x_i} + \frac{\partial \tau_{ji}}{\partial x_j} \tag{4.2}$$

$$\frac{\partial}{\partial t}(\rho E_t) + \frac{\partial}{\partial x_j}(\rho u_j H_t) = -\frac{\partial q_j}{\partial x_j} + \frac{\partial}{\partial x_j}(u_i \tau_{ij}) \tag{4.3}$$

The equations consist of the continuity, momentum, and energy equations, respectively. u is the velocity vector, ρ is the density, p is the pressure, q is the heat flux vector, τ is the stress

tensor, E_t is the total energy, and H_t is the enthalpy. The stress tensor, τ, is defined as

$$\tau_{ij} = \mu \left(\frac{\partial u_i}{\partial x_j} + \frac{\partial u_j}{\partial x_i} \right) - \frac{2}{3} \frac{\partial u_k}{\partial x_k} \delta_{ij} \tag{4.4}$$

where μ is the dynamic viscosity. The total energy and enthalpy are given by

$$E_t = e + \frac{u_k u_k}{2} \tag{4.5}$$

$$H_t = h + \frac{u_k u_k}{2} \tag{4.6}$$

where e is the internal energy and h is the specific enthalpy, $h = e + \frac{p}{\rho}$. The heat flux vector, q is defined by

$$q_j = -\lambda \frac{\partial T}{\partial x_j} \tag{4.7}$$

where T is the temperature and λ is the thermal conductivity. The system is closed using the equation of state (assuming a perfect gas):

$$p = \rho R T \tag{4.8}$$

where R is the specific gas constant [1].

As previously stated, Reynolds decomposition splits the velocity into an average and time-varying component [1].

$$u_i = \overline{u_i} + u_i' \tag{4.9}$$

For steady-state flows, the average component is given by.

$$\overline{u_i}(x,t) = \frac{1}{\Delta t} \int_t^{t+\Delta t} u_i(x,t) dt \tag{4.10}$$

For unsteady flows, Fluent uses Favre averaging for the averaged component, which involves

multiplying by the density, averaging the product, and dividing by the mean density.

$$\widetilde{u_i} = \frac{\overline{\rho u_i}}{\bar{\rho}} \tag{4.11}$$

Substituting these into equations 4.1, 4.2, and 4.3 gives the equations below,

$$\frac{\partial \overline{\rho}}{\partial t} + \frac{\partial}{\partial x_j}(\overline{\rho}\widetilde{u_j}) = 0 \tag{4.12}$$

$$\frac{\partial}{\partial t}(\widetilde{\overline{\rho}}) + \frac{\partial}{\partial x_j}(\overline{\rho}\widetilde{u_j}\widetilde{u_i}) = -\frac{\partial \overline{p}}{\partial x_i} + \frac{\partial}{\partial x_j}(\overline{\tau_{ij}} - \overline{\rho u_j^{"} u_i^{"}}) \tag{4.13}$$

$$\frac{\partial}{\partial t}(\overline{\rho}\widetilde{E_t}) + \frac{\partial}{\partial x_j}(\overline{\rho}\widetilde{u_j}\widetilde{H_t}) = \frac{\partial}{\partial x_j}(-\overline{q_j} - \overline{\rho u_j^{"} H_t^{"}} + \widetilde{u_i}\overline{\tau_{ij}} + \overline{u_i^{"}\tau_{ij}}) \tag{4.14}$$

where

$$\widetilde{E_t} = \widetilde{e} + \frac{\widetilde{u_k}\widetilde{u_k}}{2} + k \tag{4.15}$$

$$\widetilde{H_t} = \widetilde{h} + \frac{\widetilde{u_k}\widetilde{u_k}}{2} + k \tag{4.16}$$

$$\widetilde{h} = \widetilde{e} + \frac{\widetilde{p}}{\rho} \tag{4.17}$$

and k is the turbulent kinetic energy,

$$k = \frac{1}{2}\widetilde{u_k' u_k'}. \tag{4.18}$$

Equations 4.15, 4.16, and 4.17 are defined as the URANS equations, which are used for the transient simulations in ANSYS Fluent [1]. As opposed to direct numerical simulations (DNS) and large eddy simulations (LES), the URANS equations only model (not resolve) the turbulent structures within the flow, meaning they may not capture all the details of the unsteady flow, but they do significantly reduce computational resources. This Favre averaging generates the Reynolds-Stress tensors ($\overline{\rho u_j^{"} u_i^{"}}$), which are additional unknowns, so

the system must be closed by another equation: a turbulence model.

The turbulence model used for this study is the $k-\omega$ Shear Stress Transport (SST) turbulence model. This is a two-equation turbulence model that consists of a transport equation for the turbulence kinetic energy, k, and a transport equation for the turbulence specific dissipation rate, ω. This model was chosen because it combines models that provide accurate near-wall predictions, as well as free shear flows in the far-wall regions. It has proven to be particularly effective for flows over bumps, airfoils, and backwards facing steps, so it is likely a strong choice for the bluff body StreamVane geometries [19].

4.1.2 Computational Mesh

The computational domain extends 2 diameters (12in) upstream of the leading edge of the StreamVane and 5 diameters (30in) downstream of the trailing edge of the of the StreamVane. The walls, airfoils, and bluff body were all modeled as adiabatic, no-slip walls. The inlet was defined using the Mach number of interest, Mach 0.45, with a turbulence intensity of 5% and temperature of 15°C. To establish the appropriate grid sizing, a mesh refinement study was conducted. The average turbulent kinetic energy, turbulent viscosity, and mass flow rate were all monitored at 1 diameter downstream of the StreamVane.

To determine the appropriate grid level for each simulation, a grid convergence study was performed. The discretization error for each grid level was calculated with the Richardson Extrapolation method which was then converted into an uncertainty with Roache's Grid Convergence Index (GCI). First, the observed order of accuracy is calculated using the following equation:

$$\hat{p} = \frac{ln\left(\frac{f_3 - f_2}{f_2 - f_1}\right)}{ln(r)} \tag{4.19}$$

where f_1, f_2, and f_3 represent the parameter values calculated using the fine, medium, and coarse grids, respectively. r is the grid refinement factor, given by the ratios of the coarse to medium and medium to fine grid spacings ($r = \frac{h_3}{h_2} = \frac{h_2}{h_1}$). The observed order of accuracy is then used to calculate the GCI for each grid level using the following equations

$$GCI_{23} = \frac{F_s}{r^{\hat{p}} - 1} |f_3 - f_2| \tag{4.20}$$

$$GCI_{12} = \frac{F_s}{r^{\hat{p}} - 1} |f_2 - f_1| \tag{4.21}$$

where $\hat{p}$ is the observed order of accuracy and F_s is a factor of safety. Tables 4.1 and 4.2 show the statistics for each grid level and the results from the grid convergence study using a grid refinement factor of $r = \sqrt{2}$ and a factor of safety of $F_s = 1.25$.

Table 4.1: The sizing parameters associated with each grid level.

Parameters	Mesh 3: Coarse	Mesh 2: Medium	Mesh 1: Fine
Total nodes	1.9 million	3 million	5.1 million
Total elements	4.2 million	6.9 million	12 million
Max element size	2.4 in	1.65 in	1.17 in

According to these results, Mesh 2 was selected for all CFD simulations in this study, since it was the coarsest mesh where all the results converged below a GCI of 1%. As is shown in Figure 4.1, the mesh consisted of approximately 3 million nodes and 6.9 million grid elements, inflation layers on the walls, airfoils, and bluff body, and tetrahedral grid elements of gradually increasing size as they get further away from the StreamVane. The inflation

Table 4.2: The results from the grid convergence study, looking at the integral values of the mass flow rate, turbulent kinetic energy, and turbulent viscosity at 1 diameter downstream of the trailing edge of the StreamVane.

Parameters	Mass Flow Rate	Turbulent Kinetic Energy	Turbulent Viscosity
f_3	3.054	0.54632	4.0388e-5
f_2	3.0595	0.59689	4.322e-5
f_1	3.0622	0.60372	4.3464e-5
$\hat{p}$	2.05	5.78	7.07
GCI_{23}	0.66%	0.99%	3.34e-5%
GCI_{12}	0.33%	0.13%	1.49e-5%

layers were formed with a first layer thickness of 2x10^{-3} inches and increased in height by a factor of 1.1 as the layers advance away from the wall. This ensured a y^+ value of less than 30 across all wall, airfoil, and buff body surfaces. The y^+ value is a non-dimensional wall distance defined by

$$y^+ = \frac{u_\tau y}{\nu} \tag{4.22}$$

where u_τ is the frictional velocity, y is the normal distance from the wall, and ν is the kinematic viscosity [10]. Keeping this value below 30 ensures that the $k-\omega$ SST turbluence model resolves the near-wall region, so the large gradients at the boundaries are captured by the turbulence model [1]. The tetrahedral elements were kept fairly fine within 1 diameter of the StreamVane and became coarser outside this region to save computational expenses, since the areas farther downstream were not of great interest to the current study.

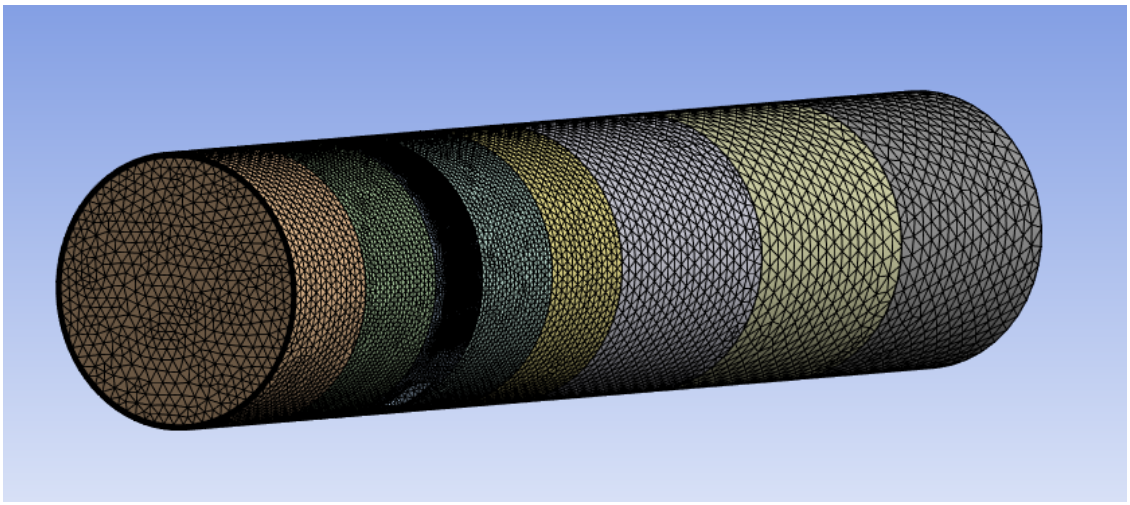

(a) The full computational domain.

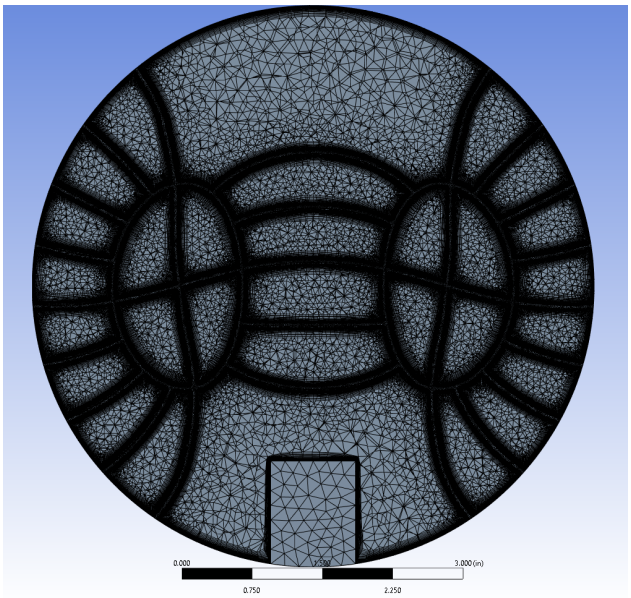

(b) A cross section of the mesh through the middle of the StreamVane.

Figure 4.1: Diagram of Mesh 2 from Table 4.1, which shows the mesh used for each CFD simulation.

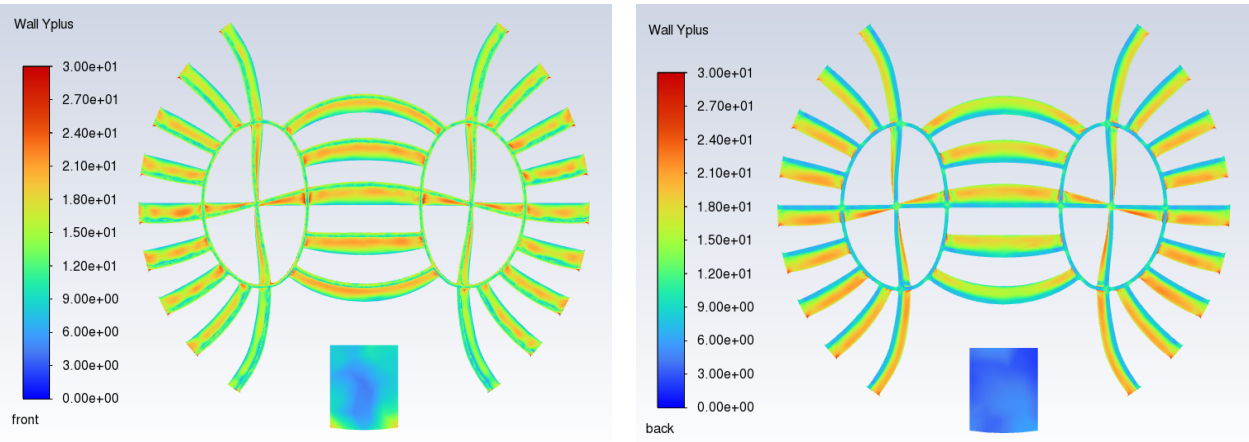

(a) Front (b) Back

Figure 4.2: y^+ values across the full StreamVane and bluff body.

4.2 Experimental Testing

Flow visualization and hot film anemometry measurements were conducted at Virginia Tech's Advanced Propulsion and Power Laboratory (APPL) using their High-Speed Wind Tunnel (HSWT). A rendering of the wind tunnel can be found in Figure 4.3. The HSWT is a suction wind tunnel that is capable of speeds of about Mach 0.5 within a 6-inch diameter test section. The tunnel is driven by a Hoffman 751 series centrifugal blower (primary blower), and a Roots-style Panther positive displacement blower by Busch Vacuum Solutions (secondary blower). The inlet flow is ingested through a flow conditioning box which eliminates large fluctuations using a series of wire mesh screens and an aluminum honeycomb. The flow goes from the flow conditioner, through a 14-inch diameter bell mouth and into the 6-inch diameter test section. Downstream of the test section, a PVC pipe exhausts the flow to the diffuser which expands the tunnel from 6-inches to 12-inches in diameter. A series of 12-inch PVC pipes bring the flow to the inlets of the two blowers. Additionally, a gate valve attached to a secondary inlet was installed between the diffuser and the blowers so the flow rate could be controlled. When the valve is fully shut, the flow is able to reach its maximum rate of about Mach 0.5. When the valve is fully open, the flow decreases to its minimum rate of about Mach 0.3. The exact minimum and maximum test section Mach numbers depend on the blockage of the test article. Since the blockage fluctuated depending on the test article, two Mach numbers were chosen as the primary flow conditions that were feasible for every design: Mach 0.45 and Mach 0.35. In order to measure the exact inlet Mach number during each run, a pitot probe was placed directly in the tunnel upstream of the test section. The pitot probe measures the dynamic pressure of the tunnel which can be converted to an inlet Mach number.

The StreamVane test articles were 3D printed using Xometry's stereolithography (SLA) printing service due to its ability to reproduce fine features, fast turnaround time, low cost,

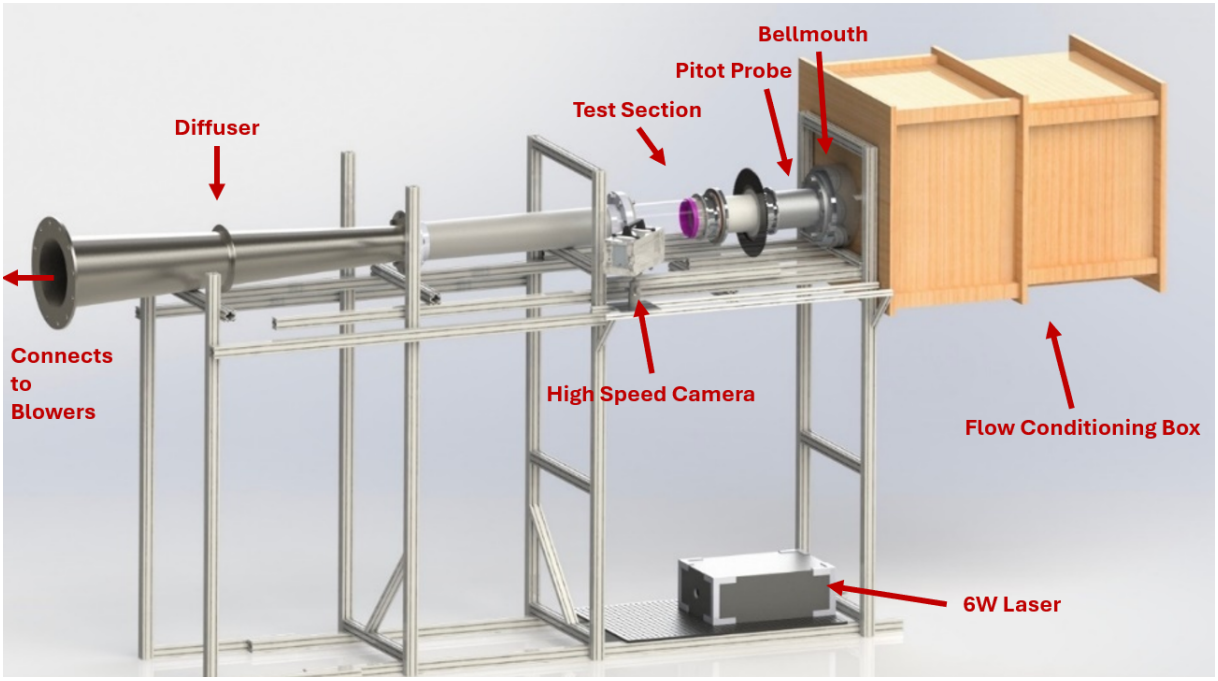

Figure 4.3: The High-Speed Wind Tunnel (HSWT) at Virginia Tech.

and wide availability of build materials. Accura® Xtreme™ White 200 and Somos PerFORM were selected as the printing material due to their relatively high strength and durability. An example of one of the models can be found in Figure 4.4. The 3D printed designs were installed into the test section of the HSWT directly downstream of the bell mouth. They were attached to a rotator section that spun on ball bearings and was powered by a stepper motor that was controlled with a LabVIEW program. This allowed the test article to rotate a full 360 degrees, which meant it could be tested at various orientations within the HSWT.

4.2.1 Flow Vizualization

For flow visualization testing, a 12-inch long quartz tube was placed directly downstream of the rotator section. The quartz tube, a photo of which is seen in Figure 4.6, allowed for visual observation of the flow one diameter downstream of the trailing edge of the test

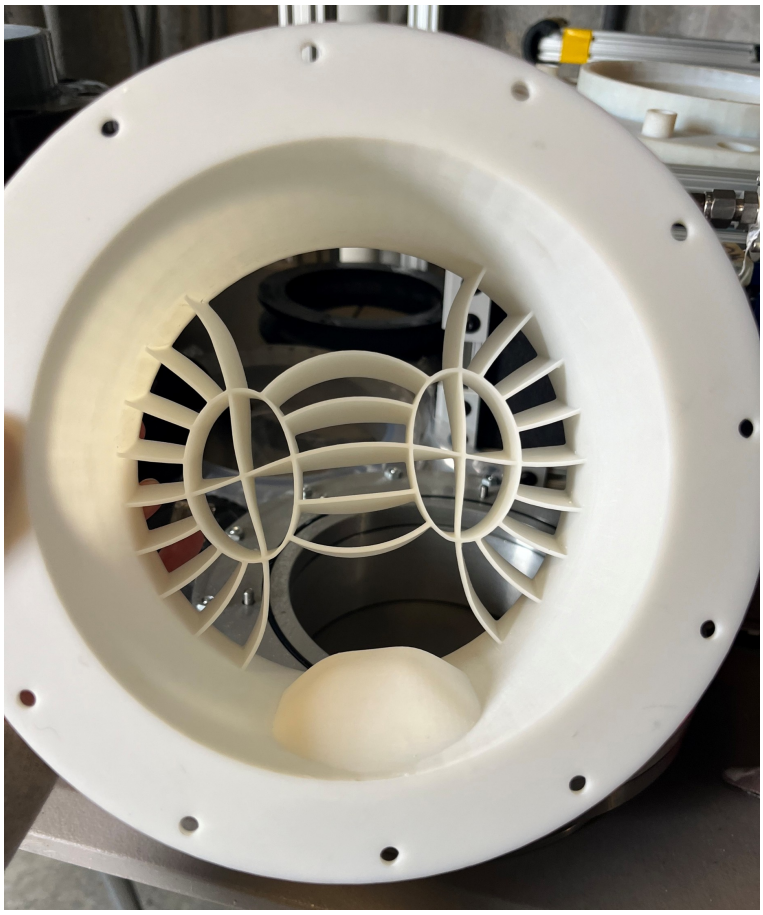

Figure 4.4: Example of a 3D printed test article (the large BeVERLI Hill design).

article. A Photron FASTCAM NOVA S12 high speed camera was mounted to the side of the optical test section and angled looking upstream to visualize the full cross section of the flow inside the quartz tube. The AIP was illuminated by a 6W, 532nm Genesis Laser that passed through a cylindrical lens to create a laser sheet. An illustration of the flow visualization setup can be seen in Figure 4.5.

Two different seeding methods were used to visualize the flow. For the higher Mach number tests, (around Mach 0.45), a steam generator was used for seeding. The steam was allowed to fill the test cell prior to and during tunnel operation so it would be sucked in through the flow conditioner and seed the test section uniformly. For the lower Mach number tests,

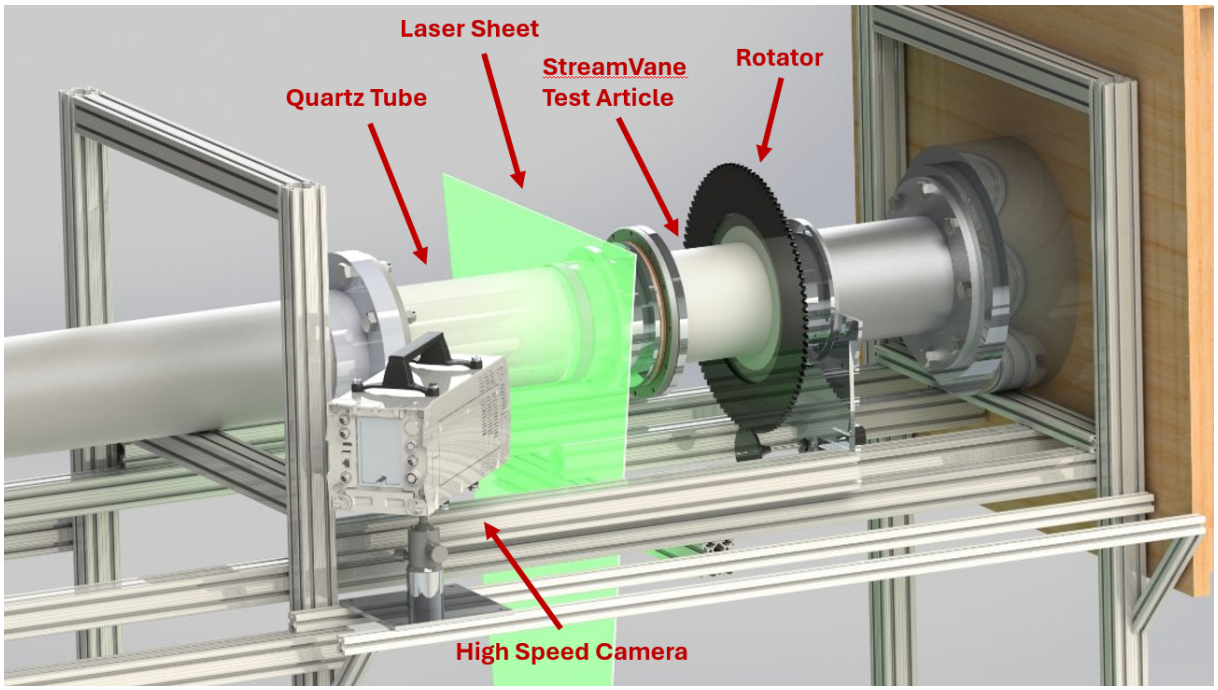

Figure 4.5: Close up rendering of the test section for the flow visualization experiment

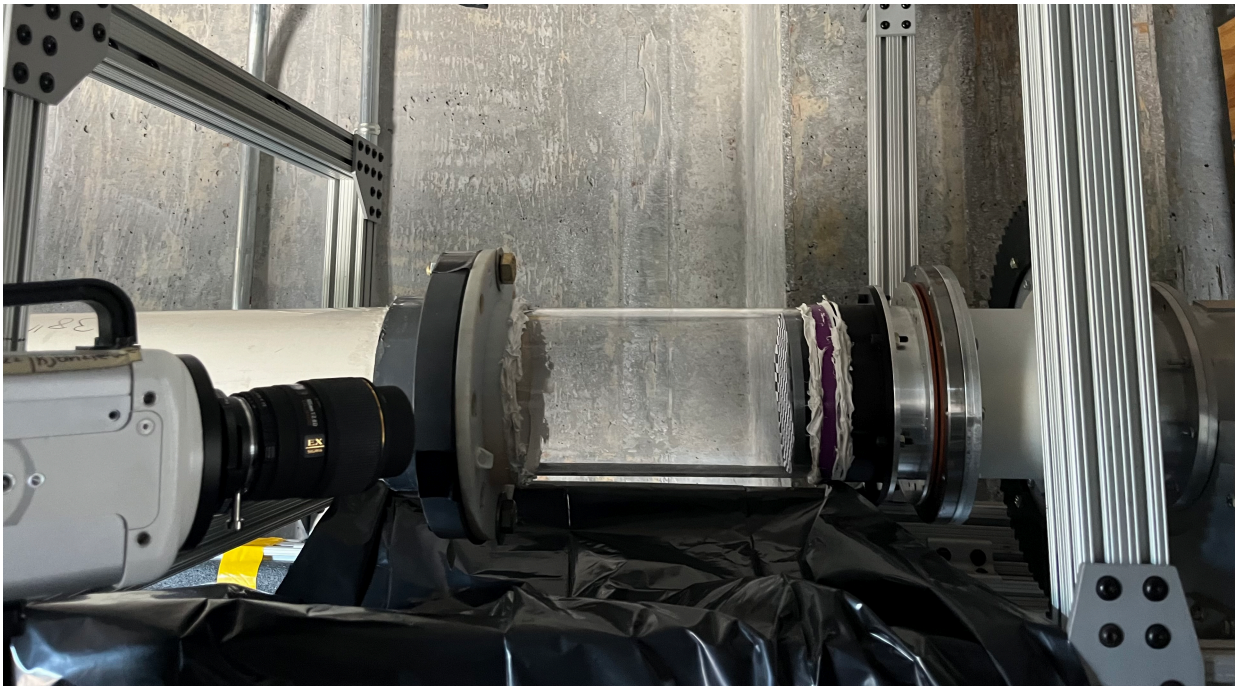

Figure 4.6: Image of the test section for the flow visualization experiment

(around Mach 0.35), a smoke generator was used to seed the test section because it filled it more thoroughly than the steam at this Mach number. The smoke machine was held behind the flow conditioner and dispersed throughout the run. When the tunnel was turned on, the smoke was drawn in through the flow conditioner and seeded the test section as uniformly as human error would allow. As the flow visualization seed passed through the AIP, it was illuminated brightly by the laser sheet, providing good contrast between the seed in the AIP and the background. The aperture of the high speed camera was kept fully open and the lens used had a 60mm focal length. Various frame rates and exposure times were tested to achieve the optimal visual data. Most data was acquired at a frame rate of 12800fps and an exposure time of 1/(frame rate).

Prior to each test, background images were collected with only the laser and camera turned on, so they could be subtracted from the wind tunnel test data and the flow features would be more prominent in the data analysis. The Photron FASTCAM viewer software showed a live view of the illuminated cross section, so there was a real-time visual of the data being collected. After background images were taken, the tunnel was turned on, and once it got up to the necessary Mach number and seeding was as uniform as possible, two 0.85 second recordings were taken at 12800fps for a total of 10897 frames in each sample. This sampling rate is well above the Nyquist frequency for the goal frequencies in the 100's of Hz range, so the full spectrum of relevant frequencies was captured and able to be analyzed.

To process the data, the background image associated with the given run was subtracted from the raw image data. Since the camera was at an angle instead of looking straight down the center of the test section, the images were also warped and resized, so they would look as if they were head-on images of the circular cross-section. The resulting high-speed videos were processed using Spectral Proper Orthogonal Decomposition (SPOD). This method attempts to decompose the unsteady motion of the seed in the video into discrete modes describing

the fundamental movement patterns. While the mode associated with the vortex shedding was not always clearly extracted, it was found that subtracting the first mode (which likely came from seeding fluctuations associated with the twin swirl vortices) isolated the relevant dynamic distortion features. Additionally, Power Spectral Density (PSD) analysis was conducted to attempt to measure the frequencies of the fluctuations due to the bluff body vortex shedding. PSD takes time-series data, in this case, the intensity of the signal of each pixel in each image over time, and decomposes it into a spectrum of frequencies and the total energy associated with each frequency. This would give information on which frequencies contribute the most to the total energy, and therefore are dominant in the flow.

4.2.2 Hot Film Anemometry

The hot film anemometry required a slightly modified test section setup in order to provide a place for the probe to be inserted into the flow. An additional 3D printed ring was added to the test section with a hole where the probe could be inserted. The hot film sensor was attached to the end of a 18 inch probe support that could move radially into and out of the test section, perpendicular to the wind tunnel, using a stepper motor controlled by a LabVIEW program. A diagram of the modified hot film test section is shown in Figure 4.7. While not necessary to the hot film measurements, the quartz tube was kept in the test section so a visual of the test article could still be seen to ensure the probe was aligned in the correct position downstream of the bluff body. The test article was still attached to the rotator so it could be oriented to a position where the bluff body was directly in line with the hot film probe and measurements of the vortex shedding would be collected.

The probe used was a TSI 1210-20 hot film sensor connected to an AN-1005 constant temperature anemometer from A. A. Lab Systems LTD. It had a length of 0.02” and a 0.001”

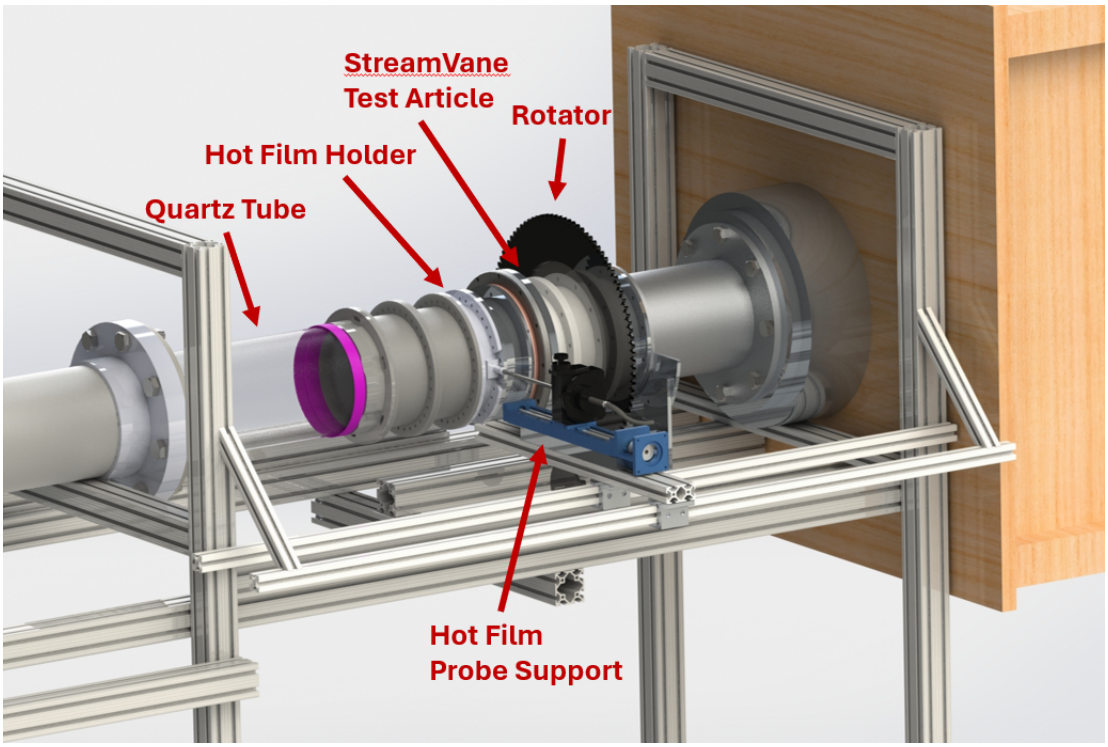

Figure 4.7: Close up rendering of the test section for the hot wire anemometry experiment.

diameter and data was acquired at 14,200 Hz for two seconds per measurement. Prior to testing in the wind tunnel, the probe was calibrated in a free jet. Since the hot film was only a single component sensor, it was not capable of resolving a three-dimensional vector of the flow velocity. Therefore, it was always oriented perpendicular to the flow in order to resolve the streamwise component of the velocity, so dynamic fluctuations due to the buff body vortex shedding could be measured.

The probe was used to measure a "pie-slice" of the flow in the area directly behind the bluff body. During each wind tunnel run, the probe was moved radially and circumferentially so it would take measurements at various locations within the area of interest. The measurements were extrapolated across the whole pie-slice area in order to get a complete contour of the flow velocity in the vicinity of the bluff body vortex shedding.

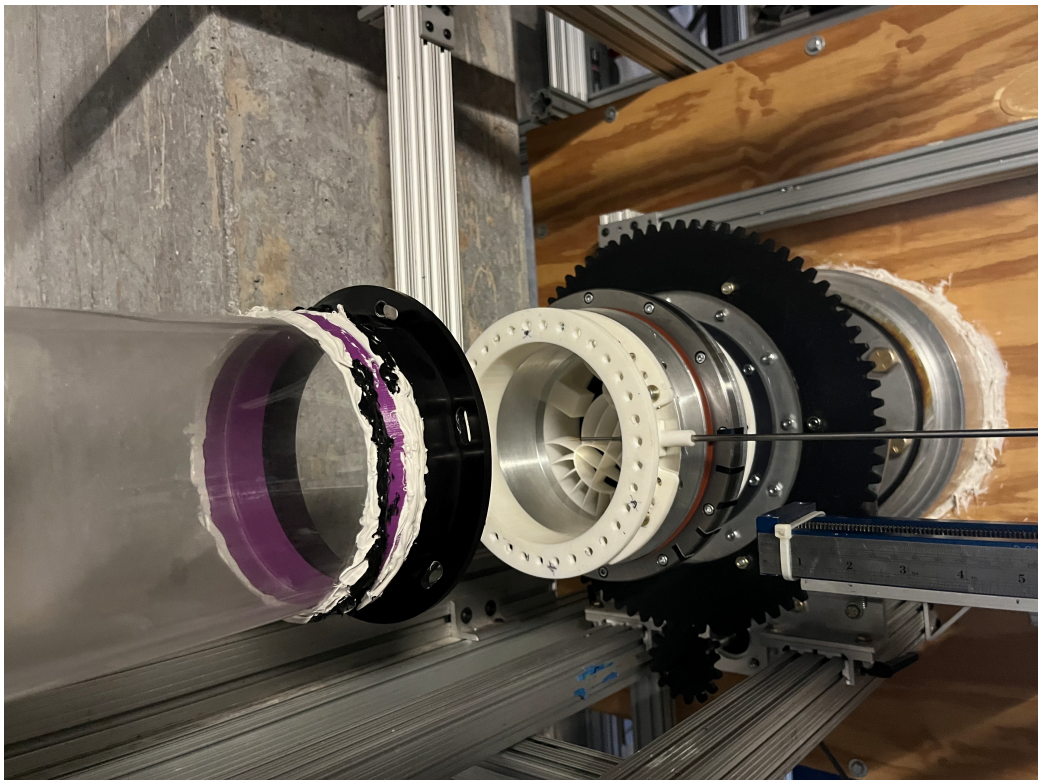

Figure 4.8: Image of the test section for the hot wire anemometry experiment. Note that the section of the wind tunnel that is absent in this image was filled with 6"-diameter 3D printed spacers. They were removed for this photo to provide an easy visual of how the test article sits inside the test section.

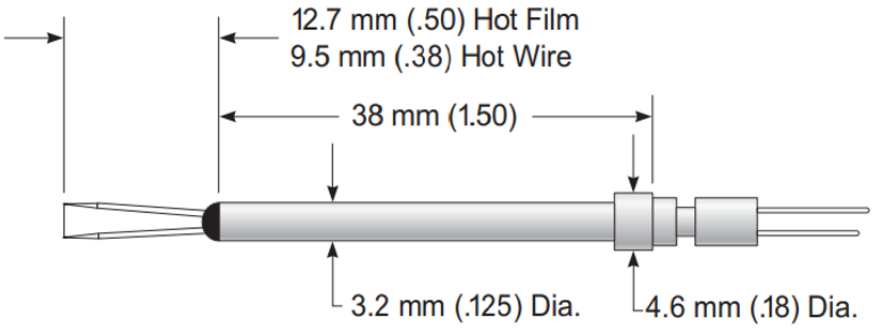

Figure 4.9: TSI 1210-20 hot film sensor used for wind tunnel testing. [25]

Chapter 5

Results

The goal of the CFD simulations and experiments was to provide evidence for the use of bluff bodies incorporated into StreamVanes in order to generate dynamic distortion. The CFD, flow visualization, and hot wire experiments were designed to give insight into the pattern and frequency of the vortex shedding from each bluff body, how the dynamics scale with Mach number and bluff body sizing, as well as understand how the secondary flow interacts with the primary twin-swirl flow.

When integrating the bluff body dynamics with the steady StreamVane profile, it was predicted that the resulting profile at the AIP would consist of the overall twin-swirl steady flow with unsteady, vortex dynamics in the region behind the bluff body. The dynamics would consist of periodic fluctuations, consistent with the type and frequencies of the vortex shedding outlined in Table 3.1. For the square prism geometries, this frequency is defined by the Strouhal number, characteristic length, and aspect ratio. For the BeVERLI Hill geometries, a chaotic switching of vortices off the back side of the hill is expected to occur. The frequencies at which these vortices shed would scale with Mach number and the characteristic length scale according to Equation 3.1.

An additional interest of this study is how the vortex shedding pattern is affected by the steady twin swirl pattern. This will give insight into what to account for when integrating a bluff body into real-world, more specific, time-varying distortion patterns at a given AIP. It was predicted that the vortices shed from the bluff body would be carried by the mean

twin swirl flow as they move downstream. For the main designs, the twin swirl creates a downward velocity towards the top of the bluff body which then turns outwards along the wall, away from the bluff body. This means the flow will likely carry the shed vortices down and away from either side of the bluff body along the wall of the tunnel. The CFD and flow visualization tests should give a visual of how the vortices move with the mean flow downstream and over time.

It should be noted that the following results exclude the design where BeVERLI Hill was positioned on the center vane. The hills were too small to produce any significant unsteadiness to the flow, so they were not tested as extensively as the other designs. This indicates that, if using BeVERLI Hill to generate dynamic distortion, the hill should be sufficiently large to produce unsteady vortices that cause dynamics of significance.

5.1 CFD Results

5.1.1 Steady CFD

Square Prism Geometries

The computational mesh depicted in Section 4.1 was duplicated on all the geometries designed for this study and used to run a variety of CFD simulations to understand the flow dynamics of each design. The first to examine was the large square prism geometry with the inlet flow set to Mach 0.45. Figure 5.1 depicts the normalized streamwise velocity, total pressure, and streamwise vorticity contours at the cross section of the tunnel 1 inch downstream of the trailing edge of the StreamVane. The square bluff body is located at the bottom of the design. There is clearly a strong velocity and pressure gradient in the vicinity

of the bluff body, indicating the region of vortex shedding. In the vorticity contour, the vortex pair is more apparent, showing up as areas of positive and negative vorticity, which indicates a vortex pair circulating in opposite directions. This matches the predicted vortex street shown in Figure 2.3. The small square prism geometry was similarly modeled with an inlet flow of Mach 0.45. The vortex street is also apparent in the contours of Figure 5.2. The vortex street is very similar to that of the large square design, but it is clear that the vortices conformed to the size of the cylinder. Therefore the sizing of the bluff body can be manipulated to dictate how large or small the area of unsteadiness is in a given flow pattern.

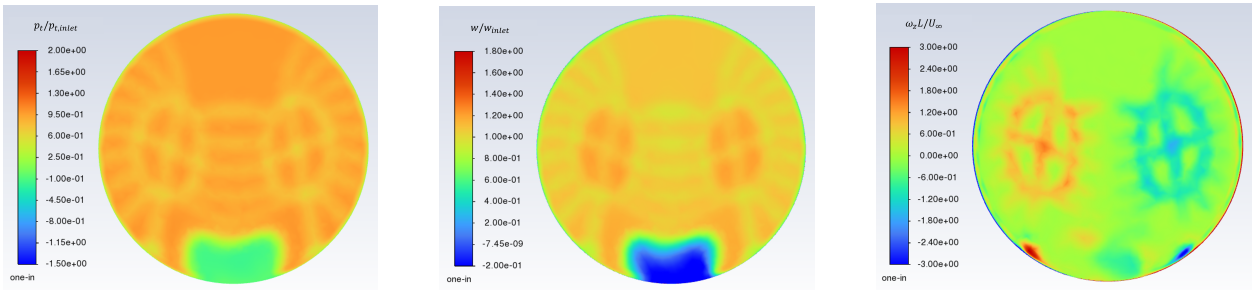

(a) Total Pressure (b) Streamwise Velocity (c) Streamwise Vorticity

Figure 5.1: (a) total pressure, (b) streamwise velocity, and (c) streamwise vorticity contours of the large square prism design at 1 inch downstream from the trailing edge of the StreamVane. The large square prism is located at the bottom dead center of the figures.

A key component to developing a Dynamic StreamVane that can produce a specific profile

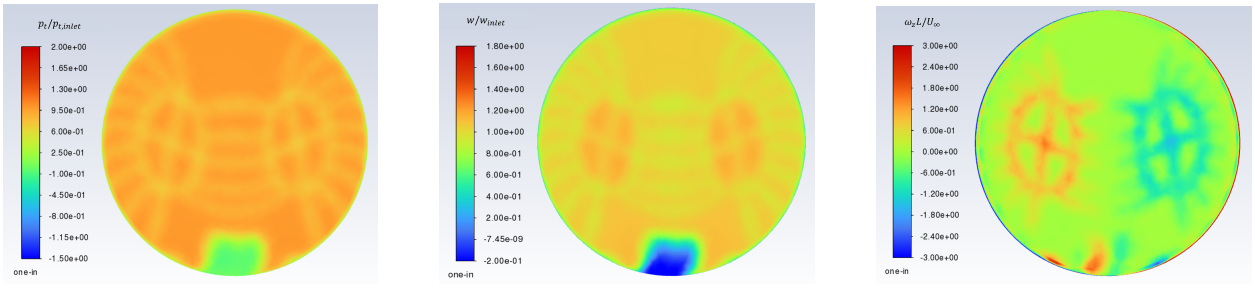

(a) Total Pressure (b) Streamwise Velocity (c) Streamwise Vorticity

Figure 5.2: (a) total pressure, (b) streamwise velocity, and (c) streamwise vorticity contours of the small square prism design at 1 inch downstream from the trailing edge of the StreamVane. The small square prism is located at the bottom dead center of the figures.

at a given AIP is understanding how the vortices evolve downstream when integrated with a base StreamVane design. It was predicted that the vortices would be carried by the main twin swirl pattern. This is confirmed when comparing Figure 5.1 to Figure 5.3, which shows the normalized streamwise velocity, total pressure, and streamwise vorticity contours at 6 inches (1 diameter) downstream of the trailing edge of the StreamVane. The large square prism is, again, located at the bottom of the StreamVane. At 1 inch downstream, the vortices are still directly behind the bluff body. However, at 6 inches downstream, they have moved outward along the wall away from the prism in either direction. This aligns with the prediction that they would be carried with the direction of the flow from the twin swirl. The strength of the vortices also appears to get weaker as they travel downstream, indicating that there is a limit to how far the unsteadiness extends.

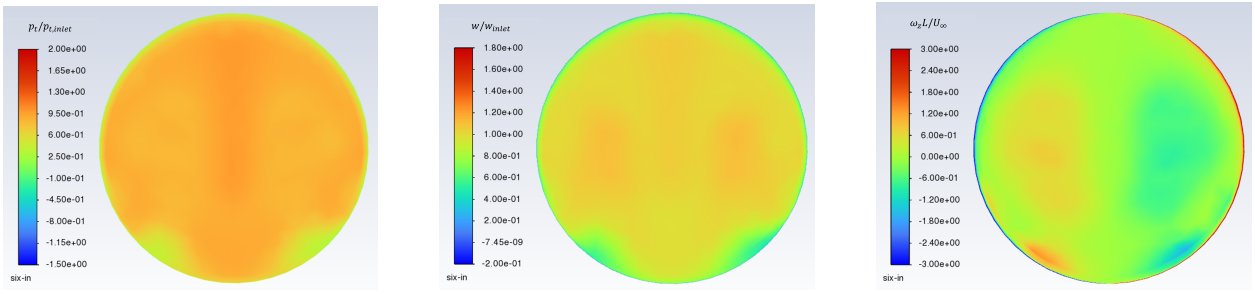

(a) Total Pressure (b) Streamwise Velocity (c) Streamwise Vorticity

Figure 5.3: (a) total pressure, (b) streamwise velocity, and (c) streamwise vorticity contours of the large square prism design at 6 inches (1 diameter) downstream from the trailing edge of the StreamVane. The large square prism is located at the bottom dead center of the figures.

The strength of the unsteadiness can also be explored by looking at the total pressure loss coefficient, which is a nondimensionalized value quantifying the pressure drop due to flow separation. From Figure 5.4, the total pressure loss coefficient peaks around 0.6 at the 1 diameter downstream AIP, which is characteristic of separated turbulent flow. This shows that there is significant dynamic behavior occurring at the AIP due to the bluff body vortex shedding, even when carried outwards by the twin swirl primary flow.

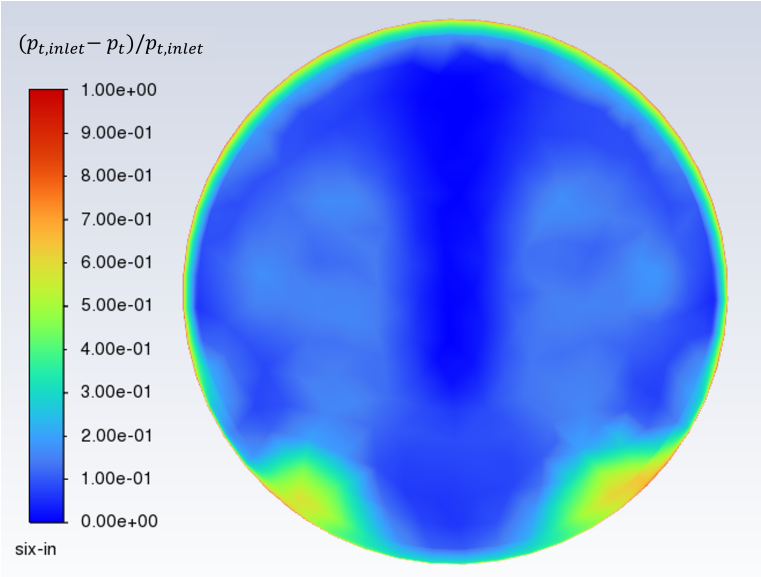

Figure 5.4: Total pressure loss coefficient of the large square prism geometry at 1 diameter downstream.

The interaction with the steady twin swirl flow is further verified when the bluff body is placed in a different location within the StreamVane. An additional design was developed with all the same parameters as the large square prism design, but instead places the prism at the top of the StreamVane instead of the bottom. While this was not one of the main geometries designed for experimental testing, this design was created to understand how a difference in location effects the evolution of the vortices as they are carried downstream. The base twin swirl pattern in this case would have the flow directed inward towards the bluff body and then travel down to the middle of the duct. In Figure 5.5, that movement is apparent in how the vortex shedding moves downstream. As the vortices move downstream, they are pulled inward and down with the direction of the twin swirl flow. Therefore, it appears that no matter where the bluff body is positioned along the shroud, the vortices get carried in the direction of the base StreamVane swirl pattern. This means there is potential to strategically place the bluff bodies in a location so their unsteady vortex streets are carried to a desired location at a designated AIP downstream.

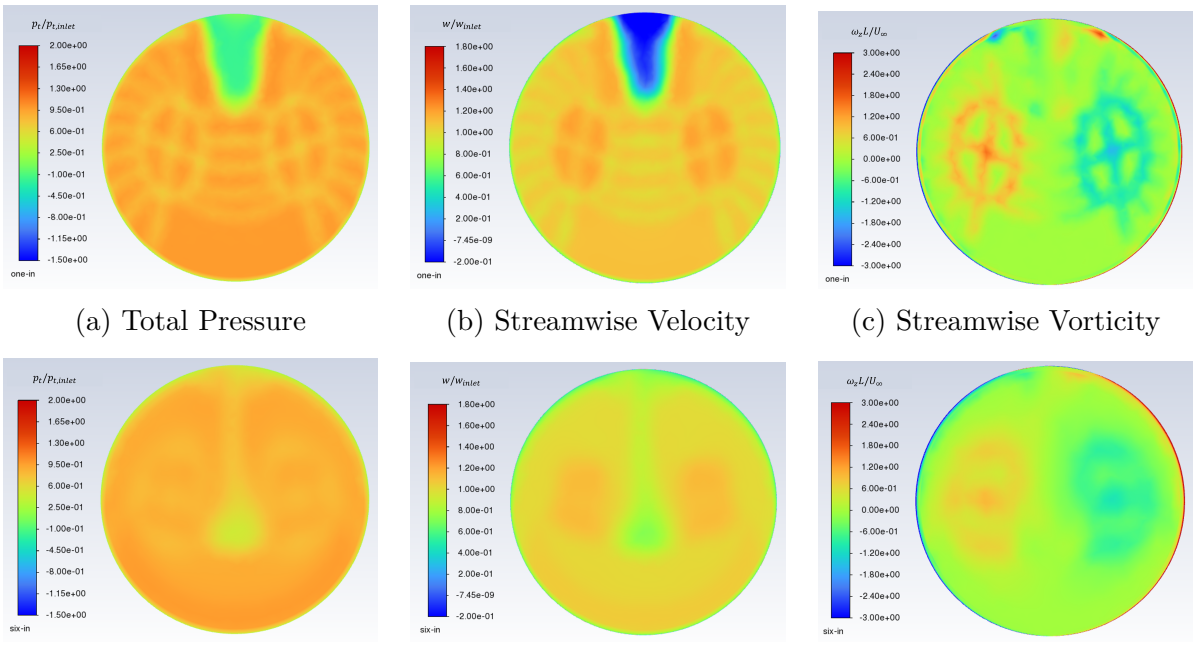

(a) Total Pressure (b) Streamwise Velocity (c) Streamwise Vorticity

(d) Total Pressure (e) Streamwise Velocity (f) Streamwise Vorticity

Figure 5.5: Contours of the large square prism located at the top dead center of the StreamVane. (a), (b), and (c) are located 1 inch downstream from the trailing edge of the StreamVane. (d), (e), and (f) located 6 inches (1 diameter) downstream from the trailing edge of the StreamVane.

Another interesting feature to note is there appears to be some level of asymmetry in the vortices shed from both the large and small square prisms. This was not expected, as typical vortex shedding from cylinders is symmetric, as shown in Figure 2.3. Without further testing, it is unclear if this asymmetry is inherent to the geometry or if it is due to imperfections in the mesh. This is definitely a feature that should be noted for future studies because, in addition to indicating a large level of unsteadiness, it will be important to consider when trying to predict the location and frequency pattern associated with cylindrical bluff bodies when developing Dynamic StreamVanes.

BeVERLI Hill Geometries

The BeVERLI Hill design was modeled with the same mesh parameters and flow conditions as the cylindrical bluff body StreamVanes. However, an additional BeVERLI Hill was added to the top of the StreamVane in order to compare the effect of placing the hill in different locations. Since the results of the cylindrical bluff bodies showed the vortices move with the direction of the twin swirl flow, it was expected that this double-BeVERLI Hill geometry would behave similarly and the hills on opposite sides of the StreamVane would not influence each other within 1 diameter downstream. Figure 5.6 shows the streamwise velocity, total pressure, and streamwise vorticity at 1 inch and 6 inches (1 diameter) downstream. While the pressure and velocity gradients are not as strong as those seen with the cylindrical bluff bodies, the vortex shedding is still clear in the areas behind the hills. There is a strong asymmetric behavior present in the vortices, especially on the bottom hill where the vortices are being pulled outward away from each other. This is consistent with previous results from BeVERLI Hill computational simulations and experimental tests. It should be noted that at 1 diameter downstream, a lot of the strength of the vortices has dissipated. This indicates that the BeVERLI Hill may not be a great choice if the AIP of interest is greater than 1 diameter downstream since it does not cause a large amount of unsteadiness at that distance downstream.

Figure 5.7 displays the vorticity, skin friction coefficient and pressure coefficient contours across the surface of the bottom hill. There is once again evidence of asymmetry in each of the contours and is especially apparent in the z-vorticity contour where the right side appears to dominate over the left. The pressure coefficient contour also greatly matches previous computational results from Gargiulo in Figure 5.7d, indicating that the same dynamics that were found in other BeVERLI Hill studies are also occurring in this study, possibly including the chaotic switching of vortices from one side of the hill to the other [5]. Figures 5.8 and

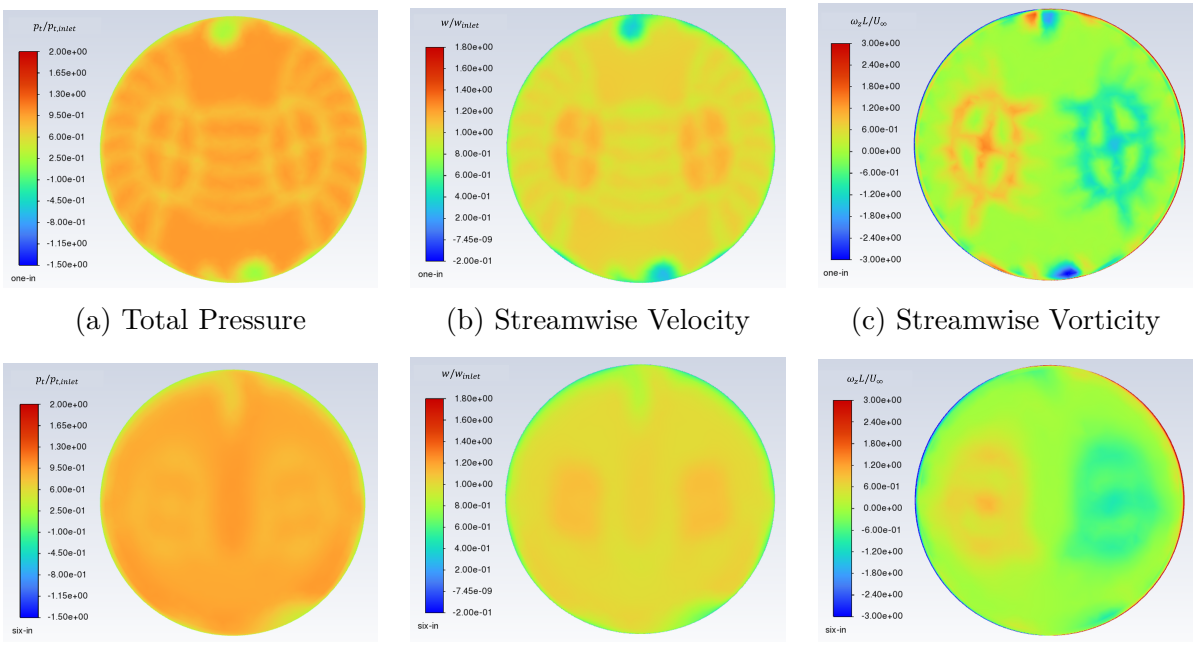

(a) Total Pressure (b) Streamwise Velocity (c) Streamwise Vorticity

(d) Total Pressure (e) Streamwise Velocity (f) Streamwise Vorticity

Figure 5.6: Contours of the BeVERLI Hill located at the top and bottom dead center of the StreamVane. (a), (b), and (c) are located 1 inch downstream from the trailing edge of the StreamVane. (d), (e), and (f) located 6 inches (1 diameter) downstream from the trailing edge of the StreamVane.

5.9 display the streamwise vorticity, total pressure, and wall shear stress from the top and bottom views of the StreamVane within the duct. From the wall shear stress contours, it is easy to see how far the vortices travel downstream before dissipating into the steady flow. Just as was indicated in Figure 5.6, the vortices just make it to about the 1 diameter mark. The wall shear stress contours also provide clear evidence for how the vortices interact with the steady twin swirl. The top BeVERLI Hill clearly shows the vortices being pulled inward, while the bottom BeVERLI Hill shows the vortices being pulled outward with the direction of the twin swirl. The contours also provide evidence for the asymmetric flow pattern that has been characteristic of the BeVERLI Hill where one side of the vortex pairing appears to be favored over the other in the steady CFD results.

As previously mentioned, comparing the BeVERLI Hill flow to that of the square prisms,

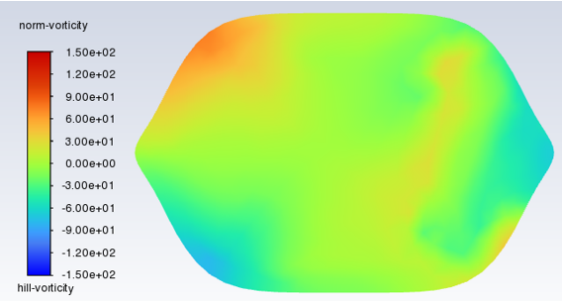

(a) Streamwise Vorticity

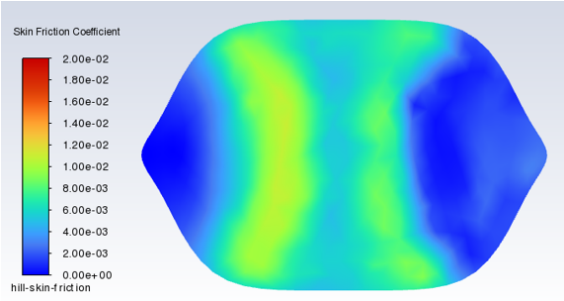

(b) Skin Friction Coefficient

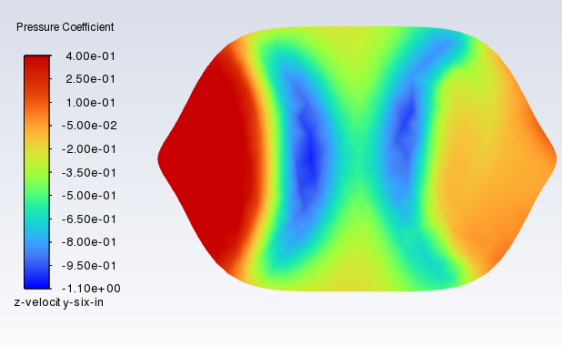

(c) Pressure Coefficient

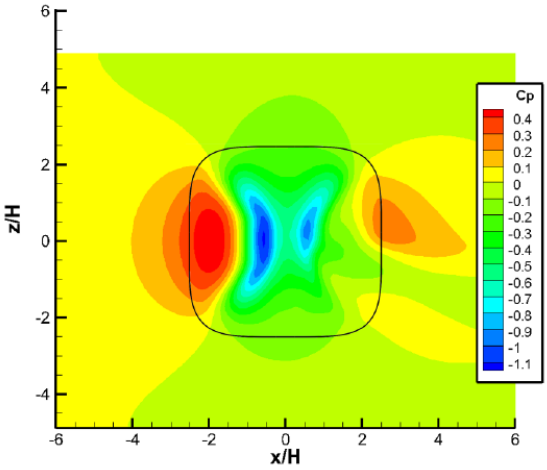

(d) Pressure Coefficient

Figure 5.7: Contours across the surface of the BeVERLI Hill located at the bottom dead center of the StreamVane. (d) from [5] serves as a comparison to (c)

the prisms clearly exhibit stronger velocity and pressure gradients. From Figure 5.10, the total pressure loss coefficient peaks closer to 0.4, which is less than the 0.6 value associated with the large square prism. This suggests that the dynamic distortion due to BeVERLI Hill is not as strong at the 1 diameter downstream AIP as that due to the large square prism. Figure 5.11 also shows that the vortices from the square prism extend farther downstream than those from the BeVERLI Hill. This provides evidence that the cylindrical bluff bodies may be a better choice for providing large unsteadiness at AIPs located farther downstream from the StreamVane.

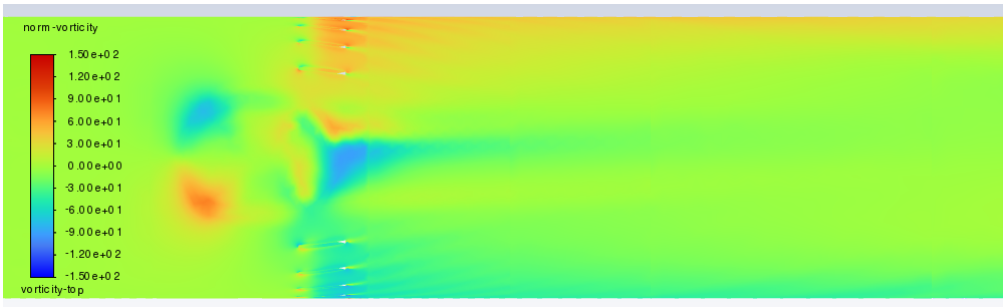

(a) Streamwise Vorticity

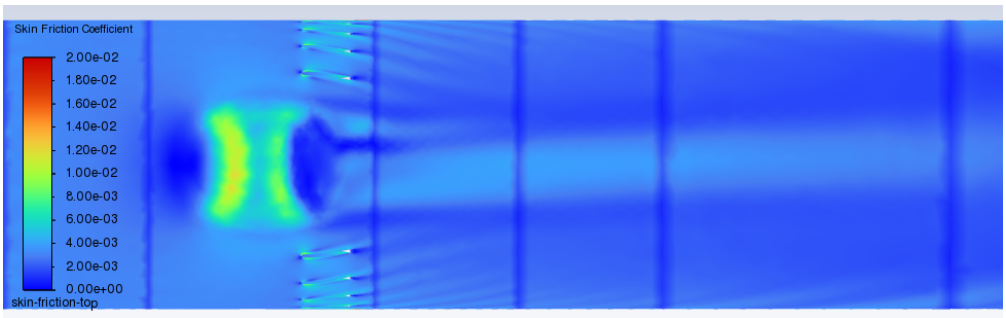

(b) Skin Friction Coefficient

Figure 5.8: (a) streamwise vorticity and (b) skin friction coefficient contours from the top down view of the computational domain of the large BeVERLI Hill design.

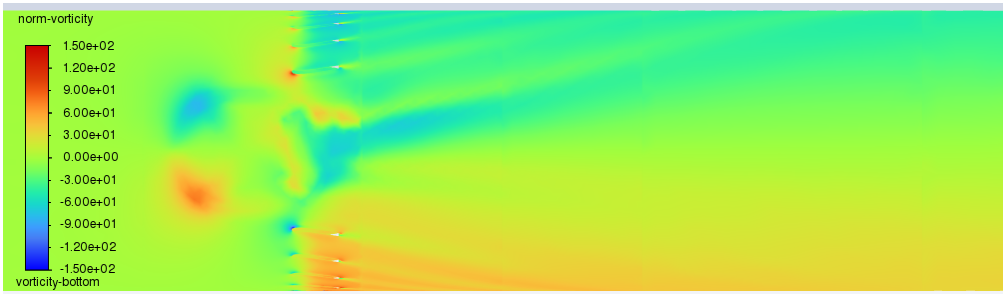

(a) Streamwise Vorticity

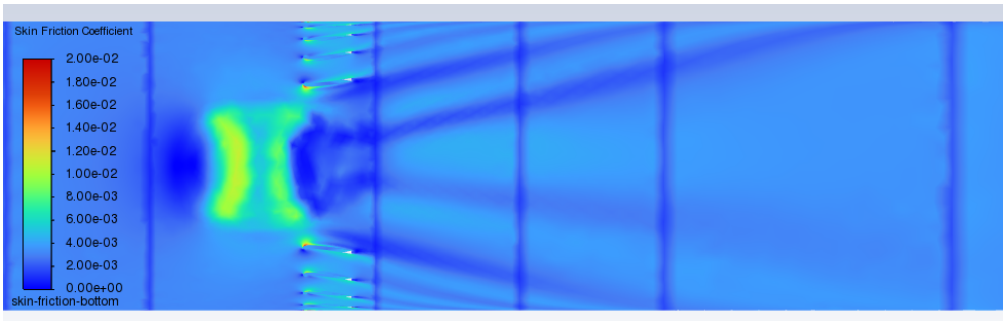

(b) Skin Friction Coefficient

Figure 5.9: (a) streamwise vorticity and (b) skin friction coefficient contours from the bottom up view of the computational domain of the large BeVERLI Hill design.

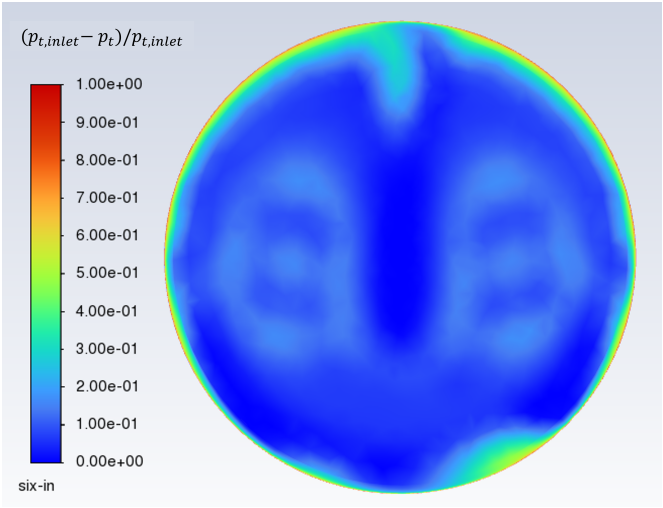

Figure 5.10: Total pressure loss coefficient of the BeVERLI Hill geometry at 1 diameter downstream.

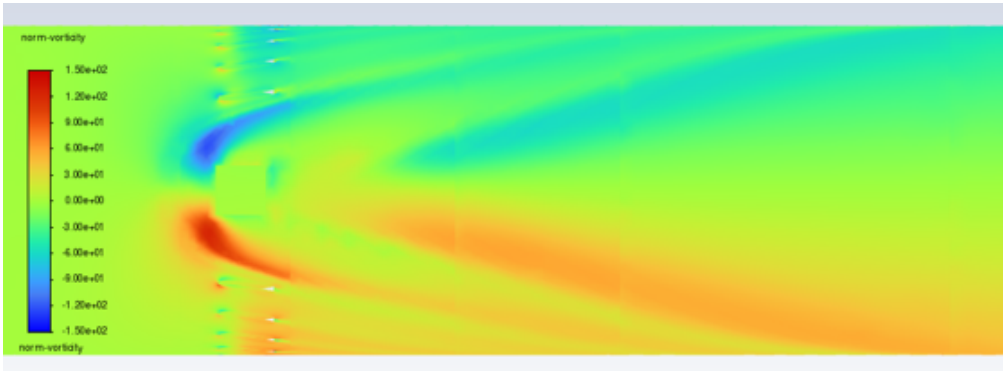

(a) Streamwise Vorticity

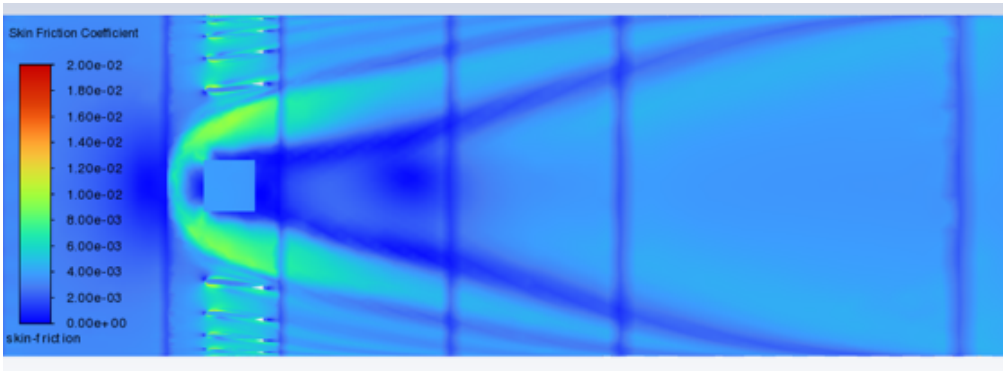

(b) Skin Friction Coefficient

Figure 5.11: (a) streamwise vorticity and (b) skin friction coefficient contours from the top down view of the computational domain of the large square prism design.

5.1.2 Transient CFD

Using the same computational mesh as the steady CFD results, a series of transient simulations were run at Mach 0.45. The goals of this study were to generate dynamic distortion using bluff bodies and understand how their vortex shedding integrates with the overall StreamVane flow. The steady results were able to show the creation of vortices due to the bluff bodies and how they move with the flow of the twin swirl. However, they did not give any insight into the type of vortex street that is generated and the frequencies at which the vortices are shed. The transient simulations are meant to fill this gap. The simulations were run for at least two shedding cycles with a time step size of 1e-6s and animations were generated of a top-down view at 0.5in from the bottom of the shroud, which corresponds to about halfway up the height of each bluff body. Therefore, in addition to seeing the dynamics at the AIP, we are also able to see the vortex dynamics down the full length of the duct.

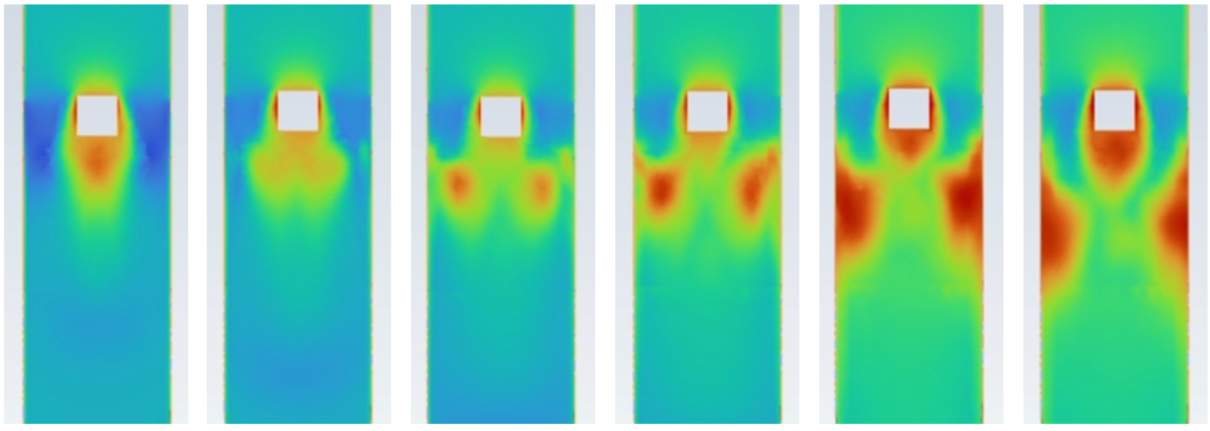

Figure 5.12: A time series of velocity contours of the large square prism design at 0.5in above the base of the shroud. These are oriented so the inlet is at the top and outlet is at the bottom.

The first design that was run was the large square prism StreamVane. According to the

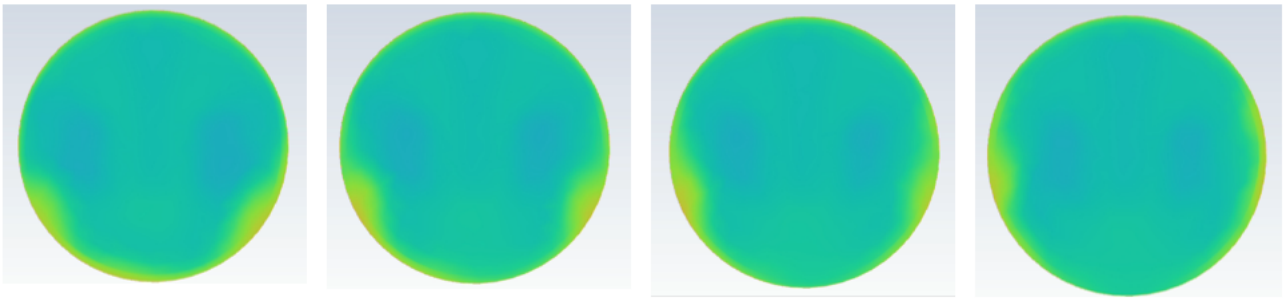

Figure 5.13: A time series of velocity contours of the large square prism design at the cross section 1 diameter downstream.

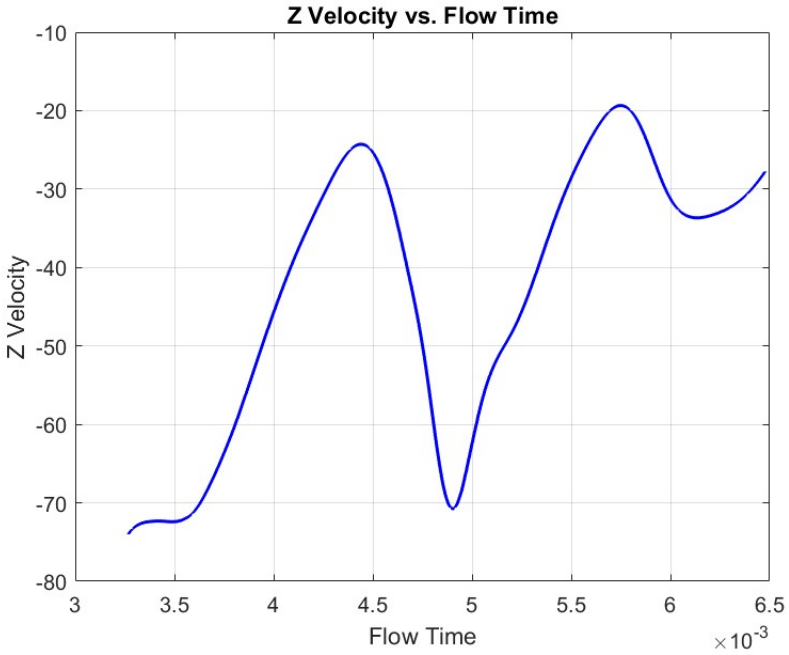

Figure 5.14: Velocity vs time in the vortex shedding region of the large square prism geometry.

calculations performed in Section 3, this design is predicted to produce arch-type vortices that shed at about 795Hz when run at Mach 0.45. Figure 5.12 shows a series of velocity contours at the cross section 0.5in above the base. It is clear that the flow separation region grows over time and a pair of vortices sheds downstream. The vortices appear to be symmetric and shed from either side at the same time, indicated that they are arch-type

vortices, as predicted. The vortices spread to the sides as they travel downstream, indicating that they move with the direction of the twin swirl flow, matching the steady CFD results. This can also clearly be viewed in the velocity contour at the AIP 1 diameter downstream, the time series of which is shown in Figure 5.13. Figure 5.13 is also clear proof that the the bluff bodies are creating dynamic distortion at a downstream AIP, as was the main goal of this research. They also appear to get disrupted when they come in contact with the wall, which confirms the idea that the unsteadiness can only extend a certain distance downstream, so the AIP cannot be too far downstream. The flow was probed inside of the vortex shedding region in order to generate the streamwise velocity verses time plot in Figure 5.14. Clearly, the vortex shedding behavior is periodic, and the frequency of this vortex shedding is about 750Hz. This closely aligns with the calculated prediction of 795Hz, indicating that the relationship of cylinder sizing to the shedding frequency may be fairly accurate in predicting the frequency content of the secondary flow.

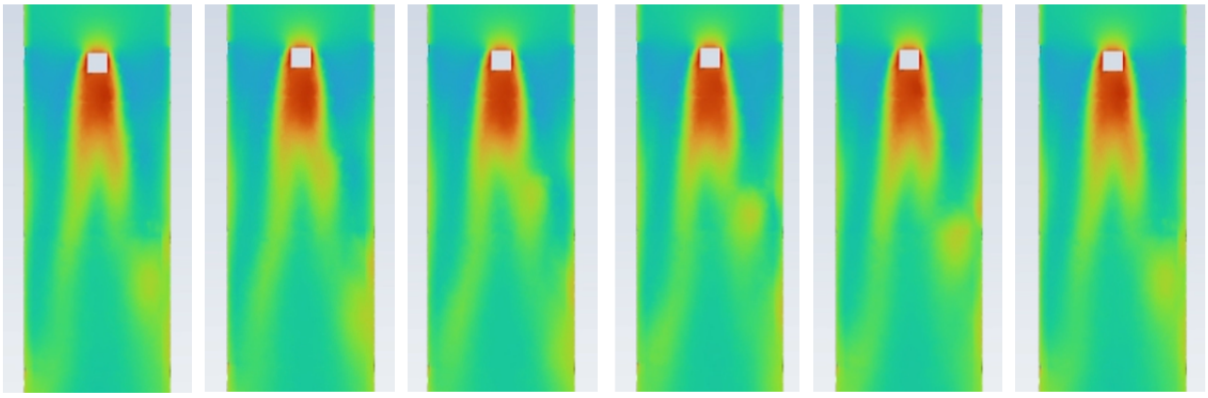

Figure 5.15: A time series of velocity contours of the small square prism design at 0.5in above the base of the shroud. These are oriented so the inlet is at the top and outlet is at the bottom.

The small square prism design was also run at Mach 0.45 for multiple cycles with a time step of 1e-6s. According to the calculations in Section 3, this design is predicted to produce Karman-type vortices that shed at about 1590Hz. In the velocity contours of Figure 5.15,

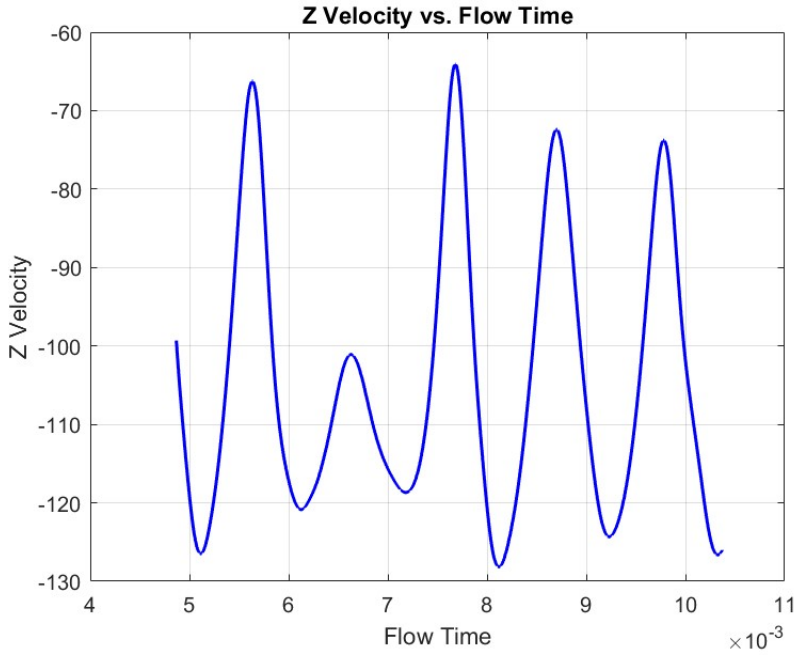

Figure 5.16: Velocity vs time in the vortex shedding region of the small square prism geometry.

we can see vortices shed downstream, but only from one side. This adds to the evidence of asymmetric vortex shedding, which is surprising from this symmetric cylinder geometry. It may also provide some support for the prediction that the prism would shed alternating, Karman-type vortices. In this case, the other side was just not captured. When comparing Figures 5.12 and 5.15, the dynamic distortion, including how the vortices shed and the size of the separation region, clearly changes with the size and shape of the bluff body. Therefore, when designing a Dynamic StreamVane to a specific distortion pattern, the bluff body can be scaled to a size that aligns with the desired dynamics. Consistent with the large square prism, for the small square prism, the vortices also move outwards as they travel downstream with the direction of the twin swirl flow. Additionally, the flow was again probed in the vortex shedding region to create the streamwise velocity verses time plot in Figure 5.16. The vortices clearly shed periodically with a frequency of about 1000Hz. This is higher than the shedding frequency of the large square prism, which aligns with the prediction that

the dimensions of the cylinder can be changed in order to produce desired vortex shedding frequencies. However, this average frequency does not align with the calculated prediction of 1590Hz using Equation 3.1. Therefore, more research is needed to determine how accurately the bluff bodies can be sized to produce the desired frequency content at an AIP.

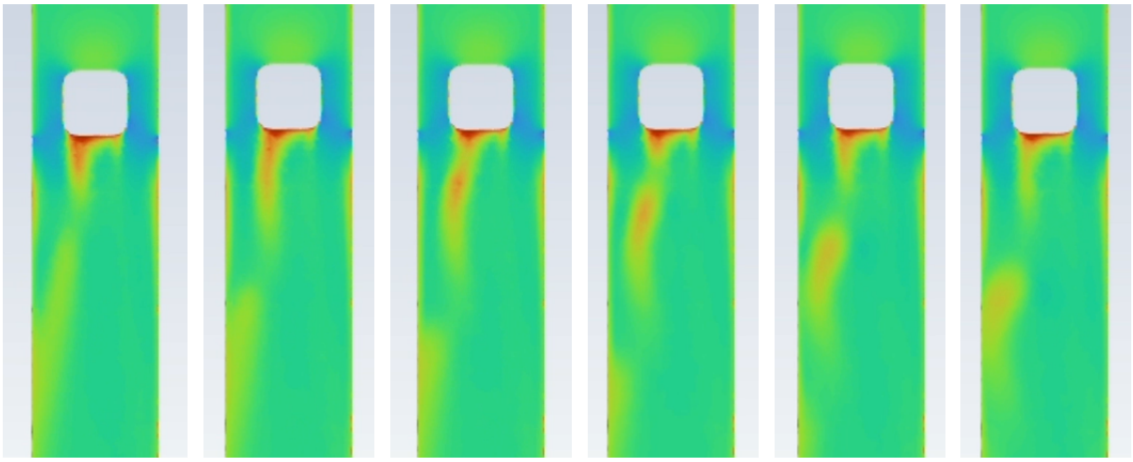

Figure 5.17: A time series of velocity contours of the BeVERLI Hill design at 0.5in above the base of the shroud. These are oriented so the inlet is at the top and outlet is at the bottom.

Finally, the BeVERLI Hill StreamVane was also run under the same conditions as the previous designs. In the contours of Figure 5.17, there is very clear asymmetry in the shedding off the back of the hill. The vortices only appear to shed off of one side in this simulation. Previously, BeVERLI hill has been found to alternate chaotically from one side to the other, so it is likely that the simulation was not run long enough to capture any switching or the computational method is not advanced enough to capture the complex dynamics of the BeVERLI Hill. While no vortex switching was captured, the vortices that are shed from the one side appear to do so periodically. The streamwise velocity verses time plot in Figure 5.18 shows that the vortices shed at a frequency of about 1000Hz. From this, BeVERLI Hill shows promise as a good, highly asymmetric dynamic distortion generator when integrated with a StreamVane. Similar to the steady RANS results, the vortices also are clearly not as

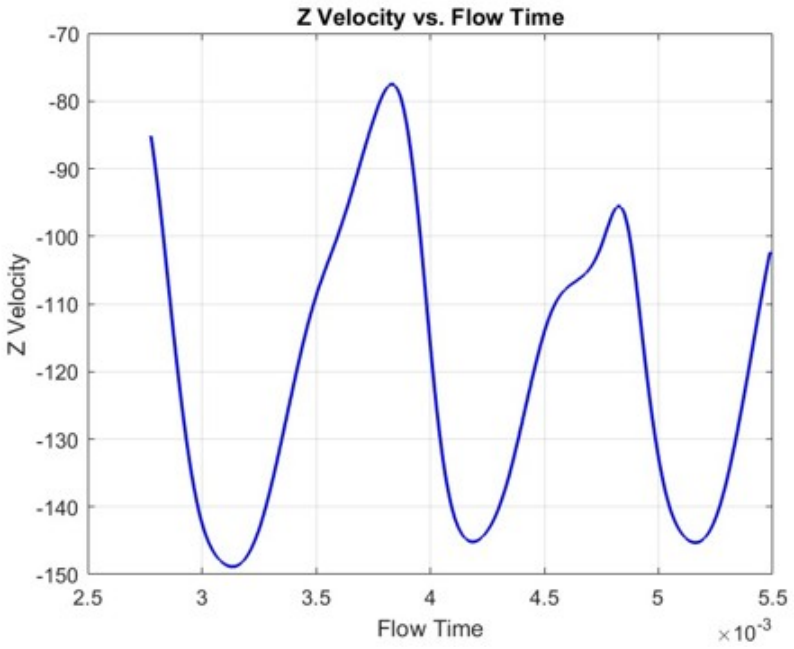

Figure 5.18: Velocity vs time in the vortex shedding region of the BeVERLI Hill geometry.

strong as they were with the cylindrical designs, indicating that BEVERLI Hill may not be the appropriate choice when wanting to produce strong, unsteady dynamics at an AIP at least one diameter downstream.

5.2 Experimental Results

5.2.1 Flow Visualization

While the flow visualization tests had complications with achieving uniform seeding, making it difficult to capture the entire flow field, the large square prism tests gave the strongest insight into the areas of interest. Figure 5.19 shows variance contours of two separate large square prism runs at Mach 0.45 at 1 diameter downstream. Both the mean and first mode were subtracted from the raw data in order to remove some of the noise and low frequency

dominant areas that came from fluctuations in seeding and natural fluctuations in the twin swirl pattern. It is clear that the majority of the variance is located in areas on either side of the bluff body, indicating that the bluff bodies are performing as expected, adding a large source of unsteadiness to the mean flow. These contours also align with the prediction that the vortices shed from the rectangular prism would be carried away from the bluff body and along the wall due to the steady flow from the twin swirl pattern. The vortices are not directly behind the bluff body, but are located farther to either side along the wall, showing they were likely carried by the twin swirl flow over the 1 diameter distance between this AIP and the trailing edge of the StreamVane. This aligns the CFD results found in Figure 5.3.

It also was predicted that the vortices and their associated variance would be symmetric across the center line of the square prism. However, the variance appears to favor one side of the prism verses the other. This asymmetry is likely due to inconsistency in the seeding at the AIP. However, asymmetry was also present in the CFD results, so there is evidence that this may be an inherent feature of the flow. The square prisms on their own are known to produce symmetric fluctuations, so further research is needed to identify whether they still produce symmetric vortices when added to a StreamVane, and whether asymmetries will need to be accounted for when designing a Dynamic StreamVane for a designated profile.

While the seeding was not as prominent in key areas for many of the runs with the small square prism, there was still a similar variance pattern captured to that of the large square prism: a large amount of the variance is concentrated to either side of the bluff body along the wall. Figure 5.20 shows the variance contour for the small square prism at Mach 0.45, 1 diameter downstream. Similar to the large square prism, there appears to be high levels of variance where predicted: the vortices were carried along the wall and away from the prism as they flowed downstream.

The behavior of the vortices shed from the large square prism are presented in the time-series

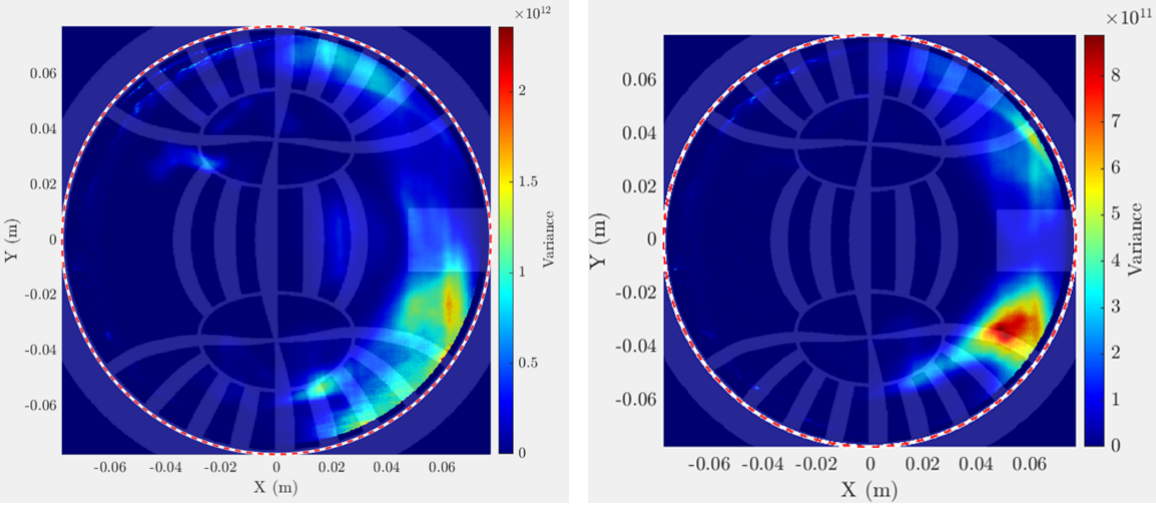

Figure 5.19: Variance contours of two separate runs at Mach 0.45 with the large square prism bluff body. Each is mean-subtracted and first mode-subtracted.

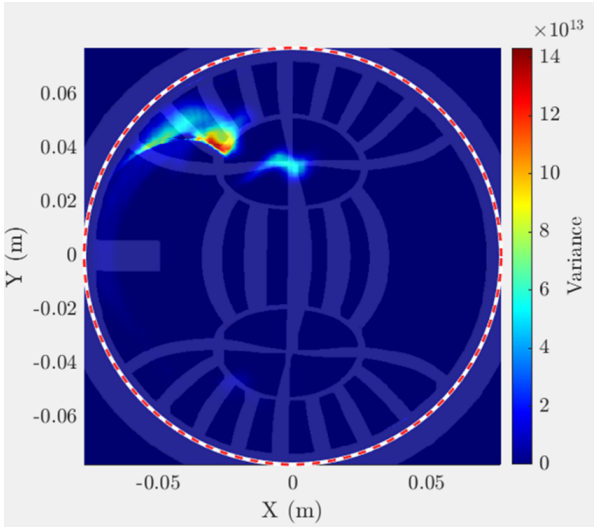

Figure 5.20: Variance contours of a run at Mach 0.45 with the small square prism bluff body. It is mean-subtracted and first mode-subtracted.

of snapshots in Figure 5.21, taken from the high-speed video. This series of frames show the vortices moving away from the bluff body along the wall, as is predicted by the direction of the flow from the twin swirl. This was a pattern that was apparent throughout the sampling period, showing that the vortices were being shed periodically and carried outward by the

steady flow over time. This gives greater insight into how these dynamic vortices interact with the steady StreamVane distortion pattern and it serves as validation for the CFD results shown in Figure 5.13. This interaction would need to be taken into account when designing a Dynamic StreamVane: the bluff body would need to be placed in a position where the vortices it sheds end up in the desired location at the AIP downstream of their original positioning at the trailing edge of the StreamVane.

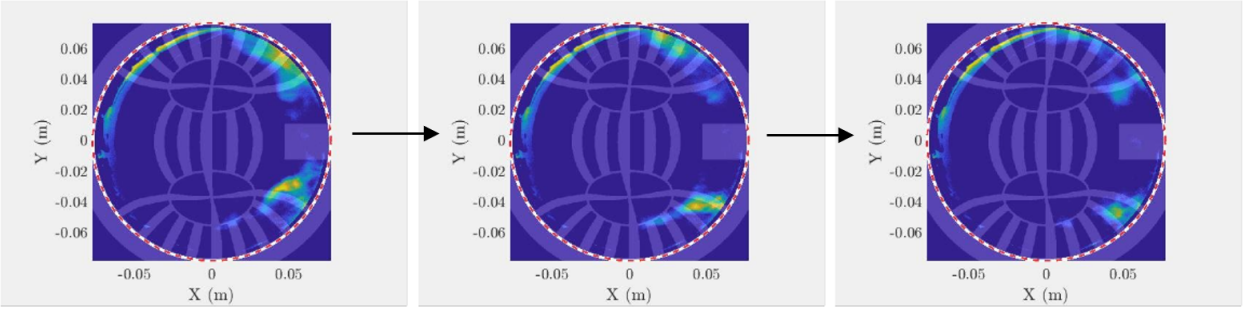

Figure 5.21: Snapshots from a run at Mach 0.45 with the large square prism bluff body. These are sequential frames showing the bottom vortex moving outward along the wall away from the bluff body over time.

One of the goals of these experiments was to confirm the predicted shedding frequencies from the bluff bodies. In order to explore this, the power spectral density of the regions where the vortices appear were calculated. Figure 5.22 and Figure 5.23 show the power spectral density at multiple locations within the vortex regions highlighted by the variance contours of Figure 5.19. The predicted frequency for this run, which was at Mach 0.45 with the large square cylinder, is 795Hz. There does appear to be a weak peak around that frequency in both of the plots; however, neither are prominent enough to draw any conclusions that they are associated with the vortex shedding. If a dominant frequency was found in the vortex regions, it would appear as a strong peak in the PSD. Therefore, it does not appear that the flow visualization tests were able to pick up any dominant frequencies associated with the shed vortices.

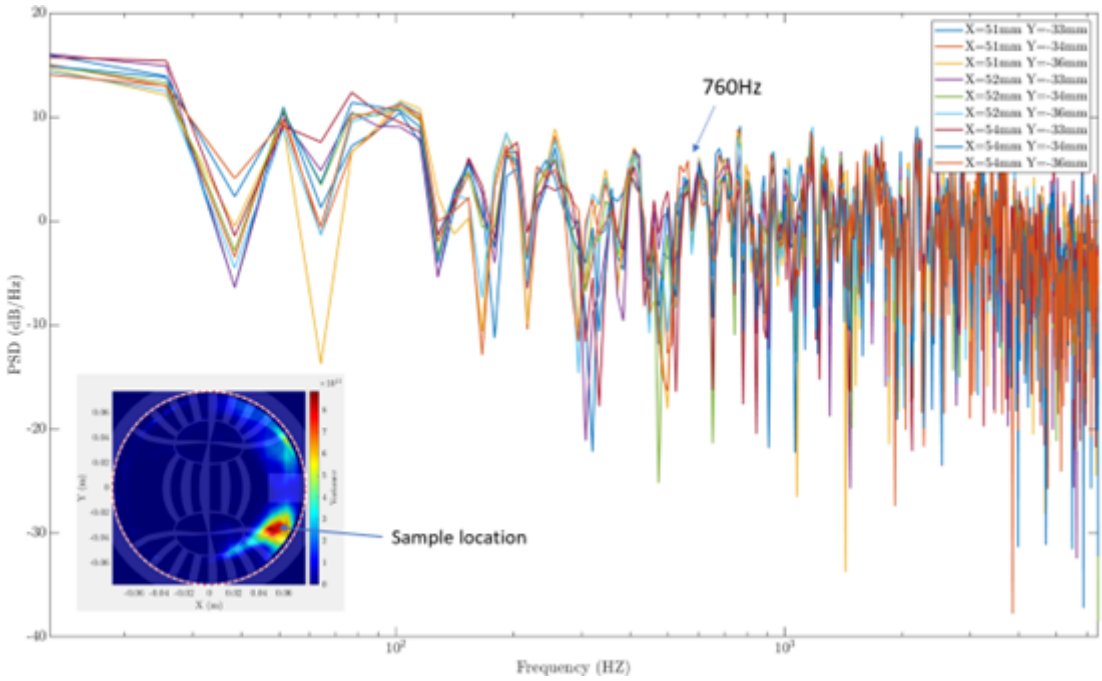

Figure 5.22: The power spectral density of a large square prism run at Mach 0.45 in the region of the bottom shedding vortex.

The same procedure was performed for the small square prism, which is predicted to have a shedding frequency of 1590Hz at Mach 0.45. However, no prominent frequency peaks were observed at that expected frequency in the area of the vortex. Therefore, there is once again no evidence of any dominant frequencies associated with the shed vortices.

Even though there were no dominant frequencies in any of these PSD plots, the majority of the energy is associated with lower frequencies. This does align with the goal of wanting to generate low frequency dynamics in the range of 1 engine order. However, there is not enough evidence to associate the low frequency dynamics with vortex shedding from the bluff bodies themselves. Without sufficient evidence to confirm that there is a dominant frequency comparable to what was expected from the bluff body geometries, it is not confirmed whether a bluff body can be designed to a specific size so it would generate a desired frequency when integrated into a Dynamic StreamVane.

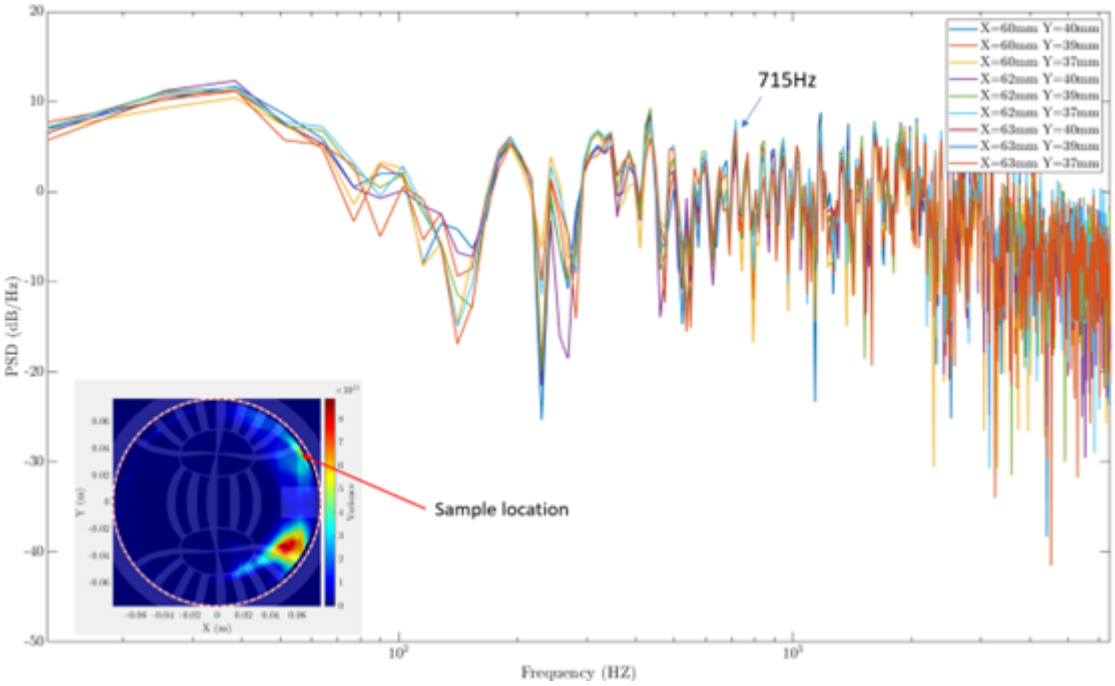

Figure 5.23: The power spectral density of a large square prism run at Mach 0.45 in the region of the top shedding vortex.

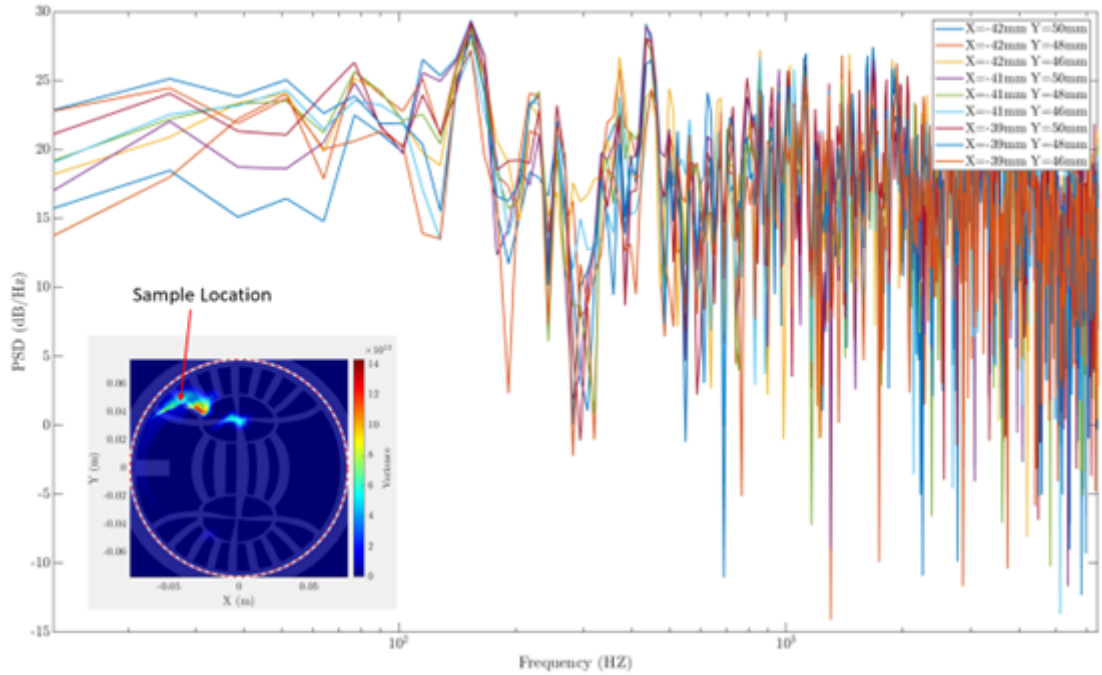

Figure 5.24: The power spectral density of a small square prism run at Mach 0.45 in the region of the top shedding vortex.

5.2.2 Hot Film Anemometry

The BeVERLI Hill StreamVanes were tested using the hot film probe to attempt to get accurate frequency sprectra of the velocity fluctuations. An array of locations were sampled downstream of the bluff body ranging from 20 degrees to the left and 10 degrees to the right of the center line of the larger BeVERLI Hill. Contours of the resulting mean and fluctuating velocity (U'/U_∞) are plotted in Figure 5.25. It was expected that most of the variance would be at the bottom corners of the sampled wedge due to the vortex shedding from the BeVERLI Hill. This is in part what the results show: the largest variance occurs at the bottom rightmost point. The least amount of variance is in a strip in the middle of the wedge above the top of the BeVERLI Hill. This is also as predicted since the vortices would likely be carried down and away from the hill by the twin swirl distortion pattern. The variance may be mostly on one side of the hill due to the asymmetric flow features associated with BeVERLI Hill. This assymetry aligns with the CFD results in Figure 5.6. However, more experimental evidence would need to be collected to validate whether an asymmetry is actually inherent to this geometry.

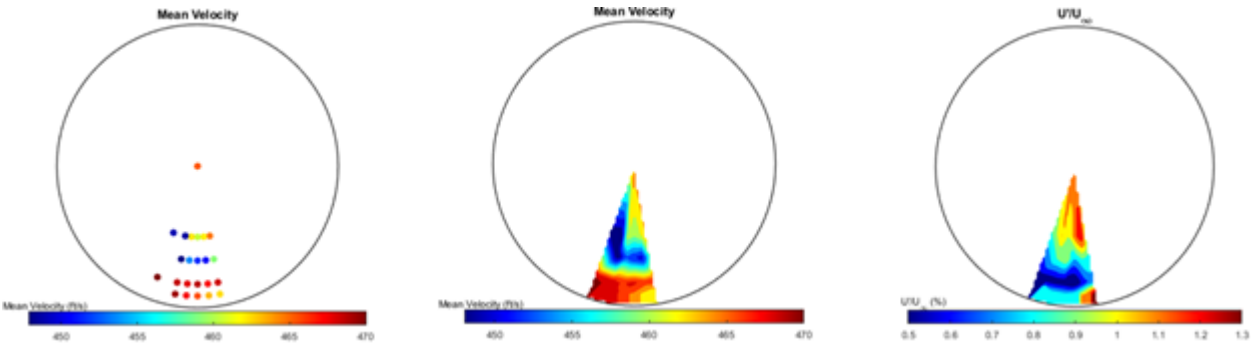

Figure 5.25: The sampling locations centered around the BeVERLI hill, 20 degrees to the left and 10 degrees to the right, and their Mean Velocity and U'/U_∞ values at Mach 0.45.

Power spectral densities were calculated at locations of high and low variance in the contour of Figure 5.25. The low variance region acts as a baseline noise level, while the difference

between this and the high variance region gives the signal due to the bluff body. As is shown in Figure 5.26, there is a signal to noise ratio of about 10 between the two spectra. This suggests that the BeVERLI Hill is exhibiting vortex shedding since it is adding power to the baseline frequency spectrum in the predicted regions, and therefore is producing unsteadiness in those regions.

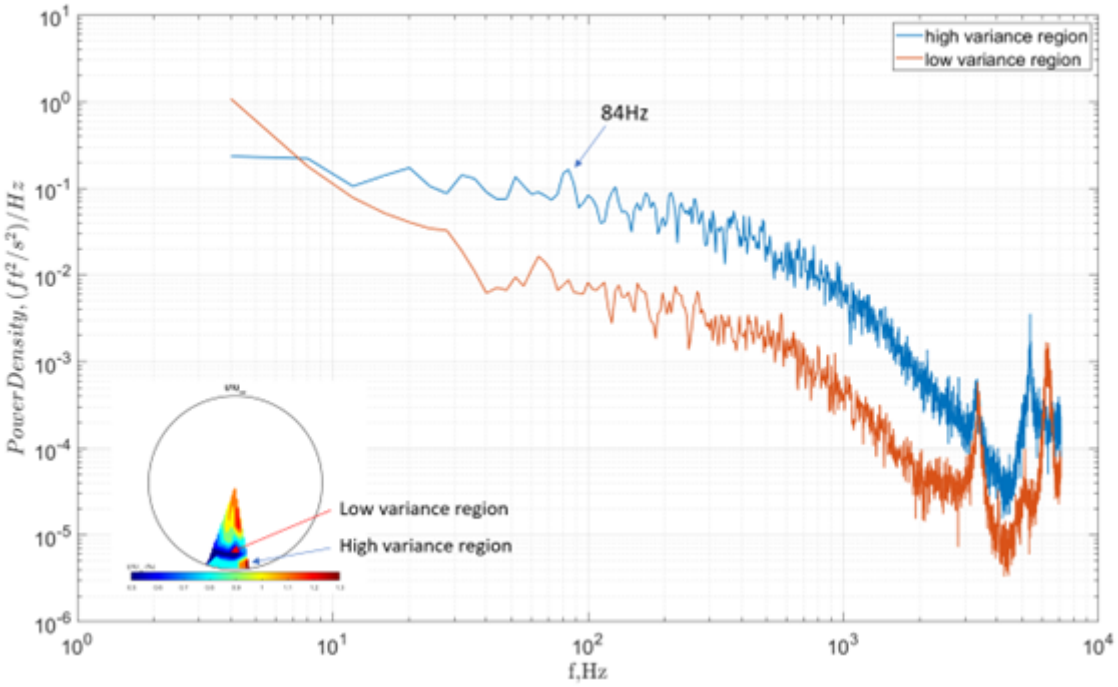

Figure 5.26: PSD of a low variance region verses a high variance region.

A similar analysis was performed on a run at Mach 0.35. Samples were taken at locations up to 10 degrees in either direction of the center line of the BeVERLI Hill, as presented in Figure 5.27. Similar velocity and variance patterns occur to those at Mach 0.45. The bottom right corner has the highest variance while the center region above the hill has the lowest variance. This suggests that there is a vortex being shed in that region of high variance which may also be exhibiting inherent asymmetric behavior.

The power spectral densities of the high and low variance regions are also presented for this run in Figure 5.28. Similar to the Mach 0.45 case, there is a signal to noise ratio of about

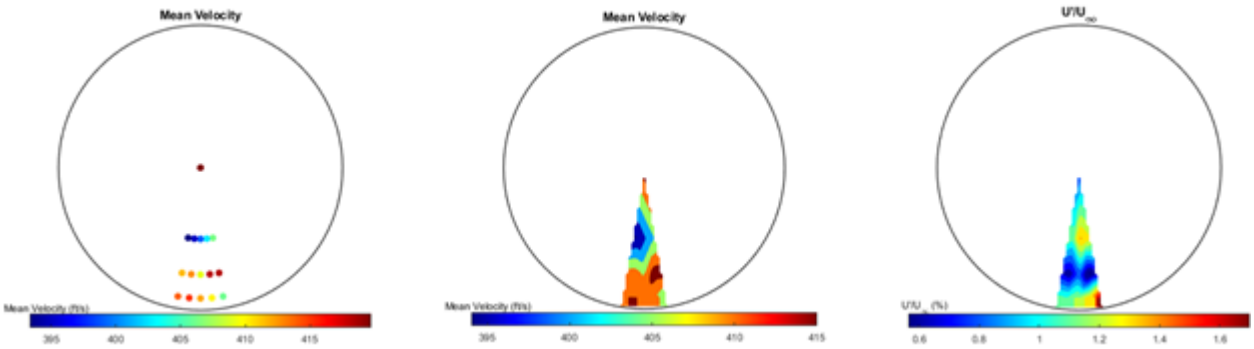

Figure 5.27: The sampling locations centered around the BeVERLI hill, 10 degrees to the left and 10 degrees to the right, and their Mean Velocity and U/U_∞ values at Mach 0.35.

10, providing evidence for the influence of vortices from the BeVERLI Hill. Another notable finding from these PSD's is the scaling of the frequency peak highlighted in both figures. The Mach 0.45 case has a peak at 84Hz while the Mach 0.35 case has a similar peak at 68Hz. It was predicted that the frequencies would scale with Mach number according to Equation 3.1. In this Mach 0.45 verses Mach 0.35 case, the frequencies should scale down by a factor of about 78%. This is consistent with the peak frequencies highlighted in the two spectra: 78% of 84Hz is 66Hz, which closely aligns with the 68Hz peak in Figure 5.28. This provides evidence that these frequencies are physical, scale as predicted with Mach number, and therefore may be due to the vortex shedding from the BeVERLI Hill.

While there is no significant evidence suggesting the predicted frequencies from Equation 3.1 result from the bluff body StreamVanes, there is evidence that the vortex shedding occurs, and that it interacts with the steady twin swirl pattern and the Mach number as expected. The vortices move with the pattern of the twin swirl, suggesting that the evolution downstream would need to be accounted for when trying to recreate any specific time-varying profile in the future. Additionally, there is some evidence that the shedding frequencies scale with Mach number as expected, so the standard relationship between Mach number and bluff body vortex shedding may be used to scale the frequencies to fit a desired profile.

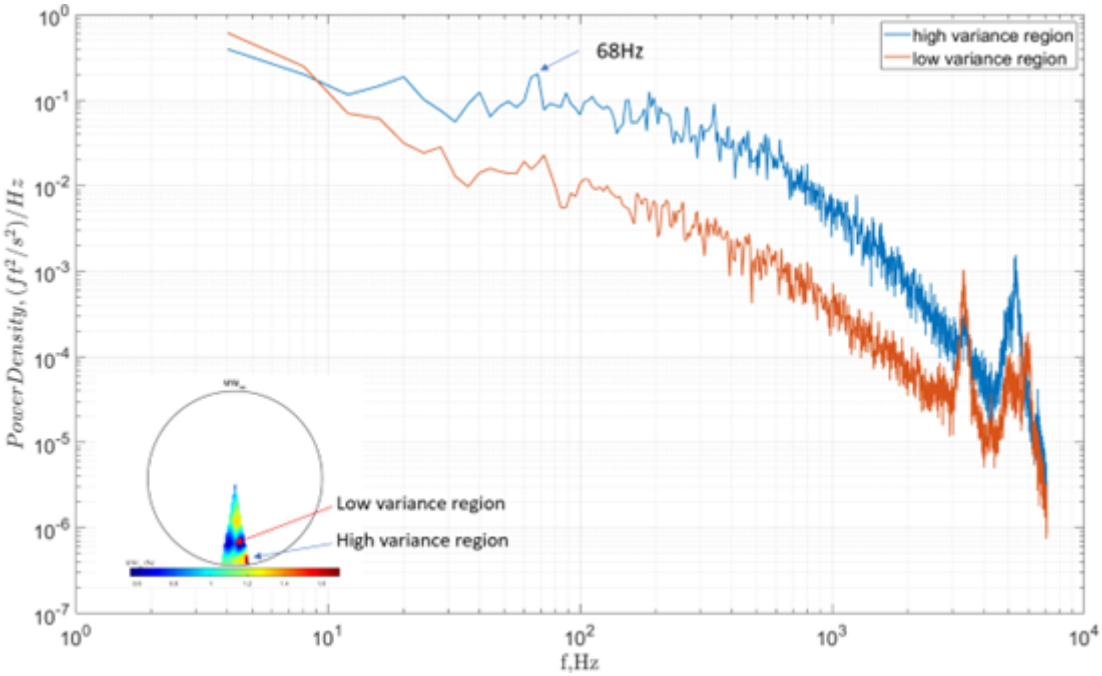

Figure 5.28: PSD of a low variance region verses a high variance region in the Mach 0.35 case.

Chapter 6

Conclusions

6.1 Discussion of Results

Serpentine diffusers generate secondary flows in the form of counter-rotating vortices that fluctuate at relatively low frequencies and cause decreased efficiency and instabilities. Due to their increased use in aircraft, there is a need for the ability to perform engine tests under dynamic distortion conditions. SteamVane technology has proved to be a highly effective way of generating specific, steady flow patterns at designated AIPs. However, they are not able to produce the unsteadiness that is characteristic of many modern day S-ducts. Due to their effectiveness in steady flow generation, it is natural to try to harness that technology and modify it to develop a new generation of StreamVanes that are capable of generating dynamic distortion. This was the goal of the presented research: to provide a proof of concept for Dynamic StreamVanes which use the natural vortex shedding of bluff bodies to serve as passive, dynamic distortion generators. While just being able to generate unsteadiness is important, the designs from this study were analyzed to show whether the location, shape, and frequency content of the dynamic distortion could be controlled by manipulating various aspects of the design, such as bluff body sizing, positioning, and scalability.

Both computational simulations and experimental tests were performed on a variety of Dynamic StreamVane designs in order to analyze the effects of differences in size, shape, and location of the bluff bodies. Square prisms and BeVERLI Hill were chosen as the bluff bod-

ies to explore because square prisms have a well-known vortex shedding behavior that can achieve frequencies in the range of one engine order, and BeVERLI Hill has a unique, asymmetric, chaotic vortex shedding behavior that oscillates at very low, irregular frequencies. The vortices from both bluff bodies shed in pairs, similar to the dynamics that are present in the real-world application of serpentine inlets. Both CFD and wind tunnel experiments were used because their results could compliment each other. The CFD gives an idea of what to expect from the experiments, and the experiments help validate the CFD results and fill in the gaps that RANS simulations are unable to capture. Multiple forms of analyze on each design provided a much more comprehensive picture of the flow from the bluff body distortion generators and gave the ability to verify the results from each test.

As expected, both CFD and experimental results show a clear increase in unsteadiness in the area of the flow behind the bluff body, indicating they are shedding vortices as expected. The first topic of interest was how these vortices would interact with the base, steady flow from the twin-swirl StreamVane. The computational results were compared at 1 inch and 6 inches downstream in order to track how the vortices move over distance. As expected, each design showed the vortices beginning near the bluff body and being carried with the direction of the twin-swirl flow at 1 diameter downstream. This was a consistent result across every bluff body design and location. The flow visualization results complimented this by giving variance contours at multiple instances in time that depict the vortices moving outward in the direction of the twin-swirl flow. They also appeared to do this periodically, further supporting the idea that the vortices are being shed periodically and moving in the direction of the steady distortion pattern. It is important to understand how the vortices evolve downstream because AIPs are typically not directly at the trailing edge of the StreamVane. Instead, the development of the dynamic flow features needs to be accounted for when trying to generate unsteadiness at a specific location at a downstream AIP.

The BeVERLI Hill was originally selected because of its unique asymmetric flow features, despite its symmetric geometry. Both CFD and experimental results exhibited strong, asymmetric results where it appeared that the vortices, and their corresponding variance, favored one side over the other on average. This meant that even though this BeVERLI Hill was significantly smaller than previously tested BeVERLI hills and had part of its base cut off due to the circular shroud, it still produced flow consistent with previous computational and experimental results. While BeVERLI was expected to exhibit asymmetry, it was unexpectedly found that the rectangular prisms also may develop an asymmetric flow pattern. It is unclear whether this is an inherent phenomenon to the design or if it was just due to imperfections in the computational mesh or inconsistencies in the flow visualization seeding. However, since the asymmetry appeared in both the CFD and flow visualization results, it is worth taking note of and further exploring if the asymmetry is something that will need to be acknowleged when creating final versions of the Dynamic StreamVane. It will be important to understand whether the vortices will be shed symmetrically or not, so the flow features of the dynamic distortion can be accurately predicted for a desired profile.

One of the reasons behind using square prisms was because they have a well know relationship between their sizing and the frequency of the vortices they shed. However, this relationship was not strongly supported by the experimental results as hoped. The flow visualization experiments did not exhibit strong peaks at the expected vortex shedding frequencies. However, this is likely a result of inaccurate seeding in the flow, so further analysis would need to be conducted in order to fully understand whether the shedding frequencies are able to be predicted when integrated into the StreamVane design. Additionally, an analysis of the vortex shedding in the transient CFD results did indicate that the small square cylinder shed at a higher frequency than the large square cylinder, as predicted, so the CFD did provide some evidence of this scaling behavior, even though the exact frequencies did

not fully match predictions. The frequencies of interest in this study are in the range of one engine order because they cause the greatest instabilities in engine fans and compressors. Even though no dominant frequencies were present, both the flow visualization and hot film power spectral densities showed that the majority of the energy in the vortex regions was attributed to low frequencies. These are frequencies that are relevant to the unsteadiness associated with serpentine diffusers. Therefore, the frequency content from the unsteady vortex shedding could be of use in real-world applications.

It was also important to understand how the flow scales with various Mach numbers and cylinder size, so the unsteadiness can be produced in the desired way for any given flow conditions. The CFD simulations clearly showed that changing the sizing of the cylinder can dictate the scaling of the vortices and the area they take up. Additionally, the hot film results showed that the frequencies likely scale with Mach number as expected. Therefore, there is evidence that the frequency and area of unsteadiness can be predicted by controlling the bluff body geometry and accounting for how it scales with the inlet flow conditions.

Finally, the Dynamic StreamVane designs will need to produce a profile at a given AIP downstream of their trailing edges. Therefore, it is important to understand how the unsteady flow features evolve downstream and how far they extend. The CFD results showed that the vortices did dissipate downstream, but still contributed some unsteadiness at least 1 diameter downstream. The cylindrical designs produced stronger vortices that extended further downstream than those from the BeVERLI Hill. Therefore, cylindrical bluff bodies are likely a better choice to generate unsteadiness at AIPs that are farther downstream. There also appears to be a limit to how far the unsteadiness extends, which would dictate how far to place the StreamVane from the engine in order to generate the desired level of unsteadiness. Each of the mentioned results from CFD and experiments provide evidence for the ability to design Dynamic StreamVanes that generate given unsteady distortion profiles

at specified AIPs and flow conditions, which will allow engine tests to be conducted against real-world flow profiles.

6.2 Future Work

The current work only begins to touch the surface of the extent to which bluff body vortex shedding can be used to generate unsteady distortion patterns when integrated with StreamVane technology. In order to understand and harness the capabilities of Dynamic StreamVanes, further computational and experimental tests need to be conducted. While RANS CFD provided insight into the mean flow characteristics and how the vortex streets generally move in time, they are unable to comprehensively capture the details of the unsteady flow. Therefore, more computationally expensive CFD, such as LES, should be performed. LES would be able to resolve the unsteady vortex behavior and more accurately capture the dynamic features of the flow. This may allow for accurate estimates of the shedding frequencies that are so important to understand and predict. Similarly, the flow visualization and hot film anemometry experiments were unable to capture any dominant frequencies associated with the vortex shedding regions. Time-resolved PIV could be conducted in order to capture this behavior and verify the corresponding CFD results. Additionally, it could capture the full picture of the flow at various AIPs downstream to provide further knowledge of how the distortion evolves downstream and how the unsteady, secondary flow features interact with the base StreamVane flow.

In order to make Dynamic StreamVanes as extensively useful as steady StreamVanes currently are, the ultimate goal would be to be able to design a StreamVane that generates a given, real-world, unsteady distortion pattern. In order to get to that point, more variations in the bluff body StreamVane design need to be explored, such as changing the base StreamVane

flow pattern and playing with the scaling and locations of the bluff bodies. This would provide a deeper understanding of the extent to which Dynamic StreamVanes could be designed to match specific flow patterns. With more extensive investigations, the Dynamic StreamVane could become the next iteration of StreamVane technology that will help engine testing facilities be able to assess their technologies against a much broader range of inlet distortion patterns.

Bibliography

[1] ANSYS, Inc. Ansys fluent theory guide, 2021. Release 2021 R2.

[2] William W. Copenhaver, Michael G. List, and Chase A. Nessler. Enumerical and experimental characterization of the transient effects of a serpentine inlet diffuser part i: Experimental results. Technical report, Air Force Research Laboratory, October 2014.

[3] Charles Dalton. Fundamental of vortex-induced vibration. University of Houston, BSEE.

[4] A. Gargiulo et al. Computations of the beverli hill three-dimensional separating flow model validation cases. *AIAA SciTech Forum*, 2022.

[5] Aldo Gargiulo et al. Flow field features of the beverli hill model. *AIAA SciTech Forum*, 2021.

[6] Julie E. Duetsch-Patel et al. The beverli hill three-dimensional separating flow case: cross-facility comparisons of validation experiment results. *AIAA SciTech Forum*, 2022.

[7] Todd Lowe et al. Non-equilibrium turbulent boundary layers in high reynolds number flow at incompressible conditions: Effects of streamline curvature and three dimensionality. Position paper, Virginia Tech, 2024.

[8] A. M. Ferrar, W. C. Schneck, W. F. O'Brien, K. M. Hoopes, and J. Bailey. Design and manufacture of generalized flow profile-producing devices, 2016. Patent No. US20160012159A1, United States.

[9] Aldo Gargiulo, Julie E. Duetsch-Patel, Aurelien Borgoltz, William J. Devenport, Christopher J. Roy, and K. Todd Lowe. Strategies for computational fluid dynamics

validation experiments. *Journal of Verification, Validation and Uncertainty Quantification*, 8(031004), 2023. doi: 10.1115/1.4063639.

[10] Andrew P. Hayden. *Comprehensive Three-Dimensional Analysis of the Wake Dynamics in Complex Turning Vanes*. PhD thesis, Virginia Polytechnic Institute and State University, Blacksburg, Virginia, November 2023. PhD Dissertation.

[11] Andrew P. Hayden, John Gillespie, Cole Hefner, Alexandrina Untaroiu, and K. Todd Lowe. High throughflow streamvane swirl distortion generators: Design and analysis. *Journal of Engineering for Gas Turbines and Power*, 146(041014), 2024. doi: 10.1115/1.4063709.

[12] Cole Hefner, Stephen Guillot, John Gillespie, and Andrew P. Hayden. Flutter parameter study on a complex inlet swirl distortion generator. *ASME Turbo Expo*, 2024. doi: 10.1115/GT2024-124102.

[13] K. M. Hoopes and W. F. O'Brien. The streamvane method: A new way to generate swirl distortion for jet engine research. *49th AIAA/ASME/SAE/ASEE Joint Propulsion Conference*, July 2013.

[14] Kevin M. Hoopes. A new method for generating swirl inlet distortion for jet engine research. Master's thesis, Virginia Polytechnic Institute and State University, Blacksburg, Virginia, May 2013. Master's thesis.

[15] J.D. Hubble and R.E. Smith. Evaluation of an airjet distortion generator used to produce steady-state, total-pressure distortion at the inlet of a general electric fioi-geioo turbofan engine. Technical Report AEDC-TR-78-73, AEDC, August 1979. Technical Report.

[16] Walter O'Brien John Gillespie, K. Todd Lowe. Definition of arbitrary swirl distortions by solutions to the helmholtz equation. *AIAA SciTech Forum*, January 2019.

[17] Aaron M. Kirk, Joaquin Gargoloff, Othon K Rediniotis, and Paul Cizmas. Numerical and experimental investigation of a serpentine inlet duct. *International Journal of Computational Fluid Dynamics*, 23(3), 2009. doi: 10.1080/10618560902835558.

[18] Daniel MacGregor, Aldo Gargiulo, Julie E. Duetsch-Patel, Philippe Lavoie, and K. Todd Lowe. Mean and unsteady surface-pressure measurements on the beverli hill. *AIAA SciTech Forum*, 2023.

[19] F. R. Menter. Two-equation eddy-viscosity turbulence models for engineering applications. *AIAA 23rd Fluid Dynamics, Plasmadynamics, and Lasers Conference*, 32(8), August 1994.

[20] Hiroshi Sakamoto and Mikio Arie. Vortex shedding from a rectangular prism and a circular cylinder placed vertically in a turbulent boundary layer. *J Fluid Mech*, 126: 147–165, 1983.

[21] Darius D. Sanders and Michael G. List. Numerical and experimental characterization of the transient effects of a serpentine inlet diffuser part iii: Time resolved comparisons. Technical report, Air Force Research Laboratory, AFRL/RQTT, June 2014.

[22] Mustafa Sarioglu and Tahir Yavuz. Vortex shedding from circular and rectangular cylinders placed horizontally in a turbulent flow. *Turk J Engin Environ Sci*, 24:217–228, 2000.

[23] Katherine N. Smith. New methodology for the estimation of streamvane™ design flow profiles. Master's thesis, Virginia Polytechnic Institute and State University, Blacksburg, Virginia, December 2017. Master's thesis.

[24] A. Sohankar. Flow over a bluff body from moderate to high reynolds numbers using large eddy simulation. *Computers Fluids*, 35(2006), 2005. doi: 10.1016/j.compfluid.2005.05.007.

[25] *TSI Thermal Anemometry Probes*. TSI Inc, 2008. URL https://www.tsi.com/.

[26] Owen J.H. Williams and Alexander J. Smits. Asymmetries in nominally symmetric flows. *Annual Review of Fluid Mechanics*, 57, 2025. doi: https://doi.org/10.1146/annurev-fluid-030124-045719.